

Manuscript NPG-2016-72

Title Trajectory encounter number as a diagnostic of mixing potential in fluid flows

Authors Irina I. Rypina and Larry J. Pratt

Anonymous Referee #1

General comments The study proposes a new diagnostic for evaluation of the mixing potential of fluid flows: the trajectory encounter number. This diagnostic is for a given trajectory defined as the number of other trajectories it approaches to within a pre-defined distance during a specific time interval. The new diagnostic is demonstrated by way of two analytical flows and a data-based flow. The proposed approach is certainly of interest for mixing analyses and, due to its straightforward concept and structure, seems particularly suited for data-based studies. Moreover, the manuscript overall is well written. However, a number of scientific and technical issues arise that must be addressed in a revision in order for the manuscript to become acceptable for publication. Details are below.

Specific comments

1. Line 43: "... property exchange can take place between different water parcels ..."
Mention that this exchange happens by diffusion and therefore relies on a concentration difference between two parcels. The relevance of tracer non-uniformity and the fact that mixing potential alone may not suffice is then evident.

We have included this clarification in the revision. The last paragraph of Sec I(a) now reads: "...the presence of a mixing potential does not guarantee that the mixing of a tracer will occur: it is also essential that the tracer distribution is non-uniform, so that irreversible property exchange can take place between different water parcels during their encounters. This exchange happens by diffusion and therefore relies on a concentration difference between two parcels. Thus, the intensity of mixing would depend on both the tracer distribution and the flow..."

2. Lines 49–50: "Our method does not require the initial spacing between trajectories to be small ..." Mustn't the spacing always be sufficiently small to detect the relevant spatial features that determine the mixing properties? In other words, doesn't your method therefore require comparable spacings as other methods in order to properly capture the physics? Your examples in fact employ fairly dense spacings (see also remark below). Please comment.

We agree with the reviewer and have removed the sentence in question from the revision.

Also, additional simulations have been carried out and included in the revised manuscript, which investigate the dependence of the encounter volume on the grid spacing. The following paragraph has been added to the revision at the end of Sec II(a):

"We have carried out numerical simulations (Fig. 6) to investigate the dependence of the encounter volume on the grid size, and to come up with a rule of thumb recommendation regarding the appropriate grid spacing. Our simulations suggest that the encounter volume values (approximated by $V \approx N dV$) are relatively insensitive to the variations of grid spacing between 1/10 and 1/2 of the encounter radius (with the encounter radius being a fraction of the size of the feature of interest, as suggested by Fig. 2), and that the major effect of a coarser grid is the degraded resolution of the resulting V map, rather than incorrect V values."

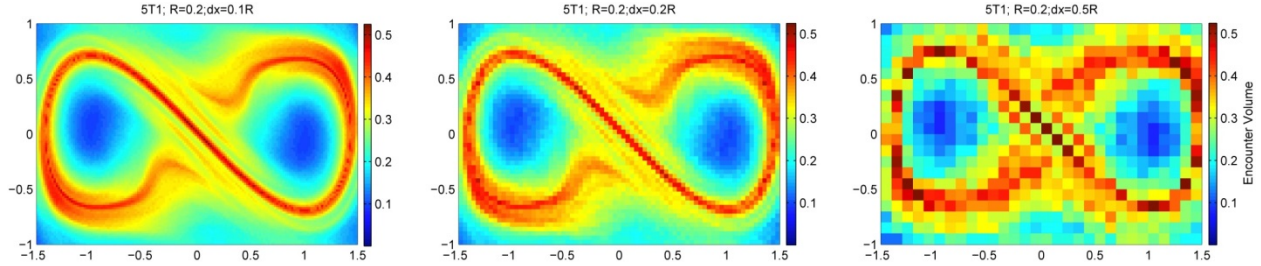


Figure 1. Encounter volume, V , for the Duffing Oscillator flow for various grids of initial positions, from dense grid spacing of 0.02 (left), to intermediate grid spacing of 0.04 (middle), to coarse grid spacing of 0.1 (right). Encounter radius, $R=0.2$, and integration time, $T=6.67$, are the same in all 3 simulations.

The emphasis on small spacing is also implied in the new text near the beginning of Sec I(b), where we formally define the encounter volume and number in the limit of infinitesimal particle spacing.

- Lines 62–67: encounter number \mathcal{N} is determined by the *first* encounter of a given trajectory with other trajectories. This relies on the assumption that in the absence of sources/sinks “most property exchange will occur during the first encounter” and in other cases “... the number of first encounters ... should still be relevant.” This is a rather loose argumentation. May the concentration difference between parcel A and B (also in the absence of sources/sinks) not just as well be *larger* – causing *more* property exchange – on e.g. a *second* encounter due to property exchange of parcels A and B with other parcels in between their first and second encounters? Please provide a stronger physical rationale for this first-encounter ansatz or present it more explicitly as an assumption or hypothesis.

Following the reviewer’s suggestion, in the revised manuscript we present this first-encounter ansatz as an assumption. The following sentence has been added to the revision to address this question:

“Note that this assumption may not hold if the parcels re-acquire different properties after their first encounter due to encountering and exchanging properties with other parcels. In this case, or in the case when tracer variance is being continuously introduced, it may be more reasonable to count the total number of encounters.”

- Lines 84–86: “... encounter rates ... are locally the largest near a hyperbolic trajectory and along the segments of its associated stable manifolds ...” This exclusive link with stable manifolds is unclear. Don’t the high encounter rates result from the rapid dispersion of fluid parcels due to exponential stretching in the homoclinic/heteroclinic tangles delineated by interacting (un)stable manifolds of hyperbolic points? In other words, don’t stable and unstable manifolds contribute equally to the high encounter rates in chaotic regions? Hence, it seems more accurate to correlate regions of high \mathcal{N} with such tangles instead of only with stable manifolds. Please either better explain the (assumed) role of stable manifolds or link the behaviour with chaotic tangles.

The reviewer might perhaps be referring to long integration times; in the long integration time limit, both stable and unstable manifolds densely fill the entire chaotic zone, and thus the entire chaotic zone is characterized by uniformly large encounter volume (equal to the volume of the

chaotic zone). So the reviewer is correct in saying that in the long integration time limit, there will be correlation between the entire manifold tangle and high encounter volume region.

Over short integration times, however, it is the stable manifold that acts as a pathway for bringing particles from remote regions into the vicinity of a hyperbolic trajectory, where particles stay over extended periods of time, and where many encounters occur. The unstable manifold, on the other hand, will rapidly remove a particle from the hyperbolic region, thus limiting its presence in the high-encounter region. Of course, the unstable manifolds will eventually bring a particle back into the vicinity of a hyperbolic region, but it will only do so intermittently (as the manifold will never reach the hyperbolic trajectory but instead will tangle around venturing away and coming back), and this process will require traveling along a significant portion of a homoclinic tangle (i.e., long integration time).

This exclusive link between forward-time integration and stable manifolds is not unique to encounter volume, but rather is typical for many finite-time methods, including FTLEs, which in forward time highlight stable manifold as maximizing ridges (see Fig. 2 below).

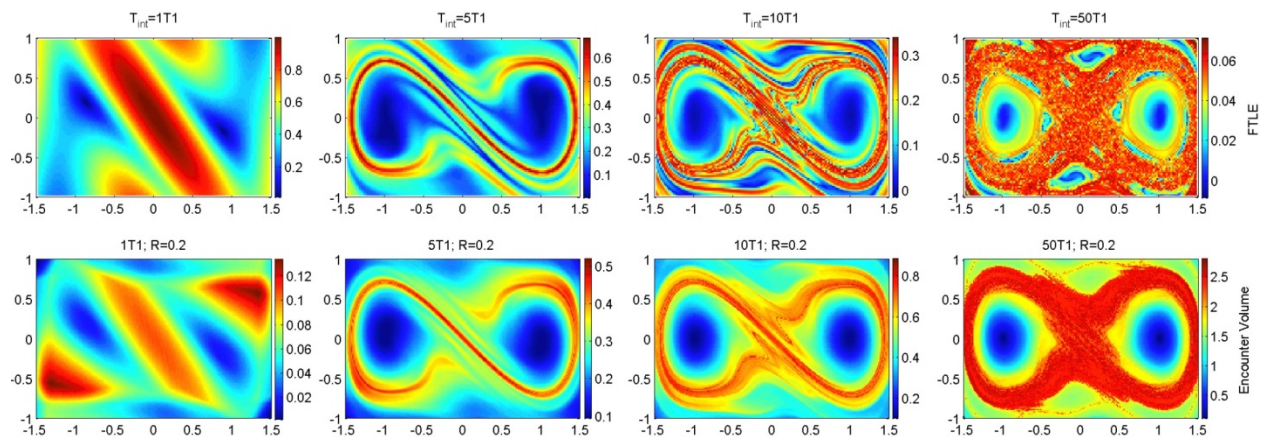


Figure 2. Comparison between the FTLEs (top) and the encounter volume (bottom; same as middle row of Fig. 2) for the Duffing Oscillator flow for various integration times, from $T=0.1T_{\text{pert}}=0.13$ (on the left) to $T=50T_{\text{pert}}=66.67$ (on the right). The same set of trajectories, deployed on a dense initial grid with 0.02 grid spacing is used in all simulations. In the bottom panels, $R=0.2$.

To further clarify this issue, we have computed both stable and unstable manifolds for the Duffing Oscillator using a direct method, where we grew manifolds from a small segment starting at the hyperbolic trajectory (which in this example stays at the origin at all times.) Both manifolds were then superimposed on a forward-time encounter volume plot (see fig. 3 below). It is clear from this new simulation that in forward time high encounter volume correlates well with the stable (and not the unstable) manifolds.

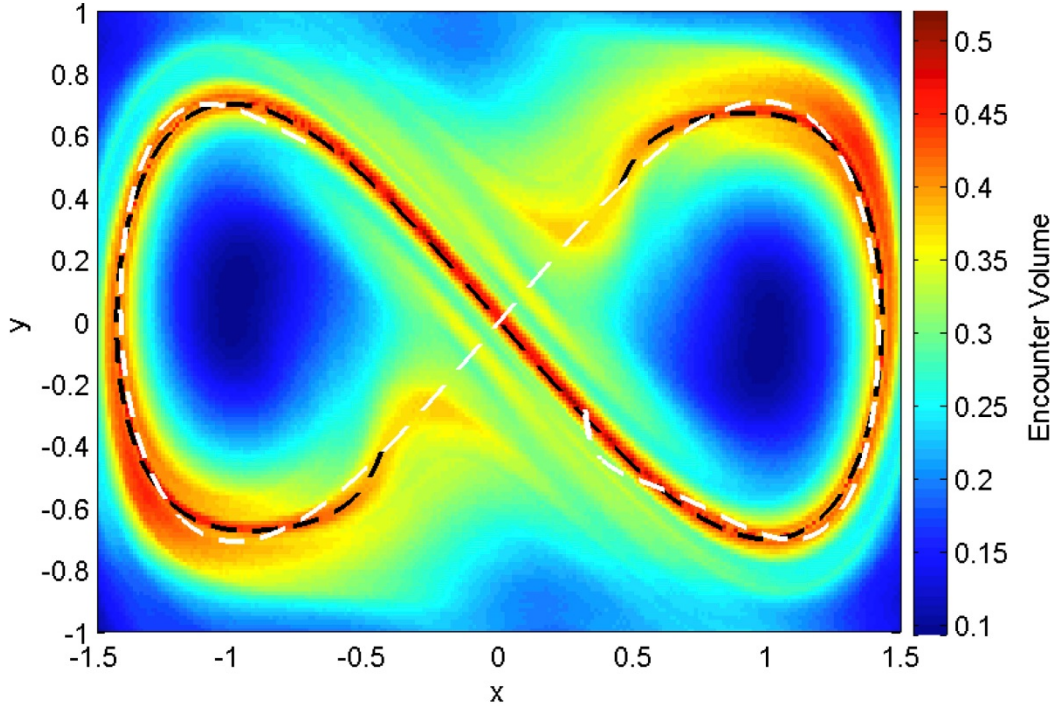


Figure 3. Encounter Volume (color; the same as 2nd row and 2nd column subplot of Fig 2 in the paper) and stable (black) and unstable (white) manifolds for the Duffing Oscillator flow.

We have added the following 3 paragraphs to Sec I(b) and II(a) of the revised paper to address this question:

“In the infinite time limit, $T \rightarrow \infty$, when all parcels within a chaotic zone (or turbulent region) of finite extent encounter all other parcels within the same chaotic zone, the encounter volume $V(\vec{x}_0, t_0; T \rightarrow \infty)$ approaches a constant equal to the volume (or area in 2d) of the chaotic zone. For 2D, incompressible flow, the encounter rates over finite T are locally the largest near a hyperbolic trajectory and along the segments of its associated stable manifolds. The stable manifolds serve as pathways that bring water parcels from remote regions into the vicinity of the hyperbolic trajectory, where parcels stay for extended periods of time, and where many encounters occur. Note that the unstable manifolds, on the other hand, will rapidly remove a particle from a hyperbolic region, thus limiting its exposure to the high-encounter region near the hyperbolic trajectory. For this reason, the unstable manifolds are not revealed by encounter volume calculation performed in forward time and require a backward-time calculation instead. This exclusive link between forward/backward in time calculation of trajectories and stable/unstable manifolds, respectively, is not specific to the encounter volume diagnostic, but rather is typical for many finite-time methods from the dynamical systems theory, including finite-time Lyapunov exponents (FTLEs), which in forward time approximate segments of stable manifold as maximizing ridges (Haller, 2002; Shadden et al., 2005; Lekien and Ross, 2010).”

“In the long integration time limit, when each manifold, either stable or unstable, densely fills the entire chaotic zone forming a dense homoclinic or heteroclinic tangle, the whole tangle will be characterized by high encounter volumes in both forward and backward time. Again, this is similar to how the maximizing ridges of the forward time FTLEs elongate and sharpen with increasing integration time.”

“In order to more clearly highlight the link between high values of V and stable (rather than unstable) manifolds, we have computed both stable and unstable manifolds for the Duffing Oscillator flow using a direct method, where we grew manifolds from a small segment starting at the hyperbolic trajectory. For the Duffing Oscillator this computation is straightforward since the hyperbolic trajectory stays at the origin at all times. Both stable and unstable directly-computed manifolds were then superimposed on a forward-time encounter volume plot in Fig. 4. The comparison shows that, as anticipated, the encounter volume diagnostic clearly highlights stable manifolds as maximizing ridges of V computed in forward time.”

5. Lines 93–94: “... will reveal longer segments of stable manifolds ... illustrated numerically in the next section.” It actually more and more seems to reveal the abovementioned homoclinic/ heteroclinic tangles instead of the stable manifolds. Consider to this end the Duffing oscillator in Sec. IIa. Here the stable and unstable manifolds of the hyperbolic point form a pair symmetric about $x = 0$ (as remarked on line 126). Their interaction yields a homoclinic tangle that delineates a figure-8 region about the two islands in Fig. 1. This tangle – and thereby *both* manifolds – coincides with the region of highest encounter rates in Fig. 2. Results on the Bickley jet in Fig. 4 further seem to support this; here correlation actually occurs with the heteroclinic tangles delineated by the interacting (un)stable manifolds of the 3 hyperbolic points instead of only with the stable manifolds. Please comment and, if necessary, modify the discussion.

Please see our answer to the previous comment and Figs. 2 and 3(Figs. 4 and 5 in the revised paper) above.

6. The discussion of Fig. 2 implies that the encounter number indeed adequately captures the dynamics. However, to this end rather smooth distributions (as e.g. in Figs. 2–4) seem necessary, suggesting that the method requires a dense spacing of initial parcel positions in order to work properly. This contradicts the statement “... does not require the initial spacing between trajectories to be small ...” (lines 49–50). Moreover, this suggests that mixing analyses by the encounter number may in fact be far more expensive than standard Poincaré sectioning (typically requiring only a few dozen parcels). Please comment and, if necessary, modify the discussion.

We have removed the sentence in question about the grid size and included numerical simulations that explore the dependence of encounter volume on the grid spacing (see our answer to comment 2 and Fig. 1 above).

We agree with the reviewer that the Poincaré section is a powerful tool for revealing regular regions and chaotic zones in time-periodic flows. We also agree that it only requires a small number of parcels. However, its application is limited to time-periodic flows, and it requires

trajectories to be computed over very long integration times, typically thousands of periods of perturbation. The encounter volume, on the other hand, is not limited to time-periodic flows, and works with much shorter segments of trajectories (longest integration time in our simulations is only 50 periods of perturbation). It also is better suited for identifying the manifolds as it does not require any apriory knowledge about the location of the hyperbolic trajectory. The encounter volume, however, requires many more parcels to be released in order to map out the phase space than the Poincare section analysis. Thus, both methods have their own advantages and limitations. We have added this discussion to the revised paper.

At the end of Sec II(a) of the revised paper, we added a discussion of advantages and limitations of the Poincare section and encounter volume methods.

“With a variety of dynamical systems techniques available, it is important to understand the advantages and limitation of the different methods. We compared the encounter volume to two well-established and commonly-used methods, the Poincare section (Fig. 3) and the FTLEs (Fig. 5). Since the Poincare section requires stroboscopic sampling of trajectories in time, it can only be applied to time-periodic flows, and requires that trajectories are computed over long integration time, typically thousands of the periods of the perturbation. On the other hand, it generally requires only a few parcels to be released at some key locations, rather than releasing a dense grid of initial positions, to map out the entire phase space. The encounter volume and FTLEs, on the other hand, are not limited to time-periodic flows, and also work with significantly shorter segments of trajectories (longest integration time in our simulations in Fig. 2 is only 50 periods of perturbation). They are also better suited for identifying manifolds than the Poincare sectioning as they do not require any *a priori* knowledge about the location of the hyperbolic trajectory. On the other hand, they require many more parcels to be released in order to map out the phase space. When applied to the same set of trajectories (same initial positions and integration times), the FTLEs and the encounter volume methods produced similar results (Fig. 5), with V being arguably better suited for 1) identifying the coherent core regions of eddies, where FTLEs have spiraling patterns that complicate the analysis, and 2) producing more continuous segments of manifolds at intermediate integration times, when FTLE-based ridges get discontinuous near the turning points of a manifold. The advantage of FTLEs, on the other hand, is that they have fewer parameters (T and grid spacing), whereas V also depends on R , and that they less expensive computationally. The more expensive computational cost of V compared to FTLEs is due to two reasons: first, the FTLEs only depend on the initial and final positions of trajectories, whereas V depends on the entire trajectory history; and second, FTLEs depend on the relative distance between a trajectory and its closest neighbors, whereas V keeps tracks of encounters with all trajectories, not just the neighboring trajectories. Thus, the cost of evaluating FTLE for each particle is independent of the total number of particles released, and the cost of evaluating V for each particle increases in proportion to the number of particles (since one needs to keep track of encounters with all particles). The calculation of V is still feasible for realistic geophysical flows, as is illustrated below. Note also that, depending on the physical question

being studied, the information about the entire trajectory, not just the final and initial position, might in fact be advantageous.”

7. The above suggests that Poincaré sectioning outperforms the encounter-number method in periodic flows. Hence, the periodic examples mainly serve to demonstrate the physical validity of the encounter-number method; its true usefulness seems to be for essentially aperiodic flows as e.g. the Gulf Stream flow (Sec. IIc). However, the analysis of this flow is rather superficial and open-ended (lines 209–230). It is recommended to deepen this analysis so as to convincingly demonstrate the potential of the method (in particular) for aperiodic flows.

Please see our answer to #6 regarding comparison and relative advantages/disadvantages of Poincaré section vs encounter volume methods.

We agree with the reviewer that the Gulf Stream flow is the most interesting from the oceanographic point of view, and in the revised paper we have extended this section. However, in-depth analysis of transport and mixing properties of the Gulf Stream Extension flow, along with the study of the Lagrangian properties, leakiness and coherence of the Gulf Stream rings, is out of the scope of this paper, and will be better suited for a separate paper that will be devoted entirely to this topic.

8. Sec. III: it is recommended to demonstrate validity of expressions (1), (2) and (9) for \mathcal{N} by comparison with \mathcal{N} found via actual parcel trajectories of the corresponding simplified flows.

We have performed numerical simulations for the linear strain and linear shear flows to check the validity of formulas (2) and (9). Numerical simulations and analytical expressions for the encounter volume are in excellent agreement with each other (see Fig. 4 below). This figure was also added to the revised paper [Fig. 10 in the revised paper].

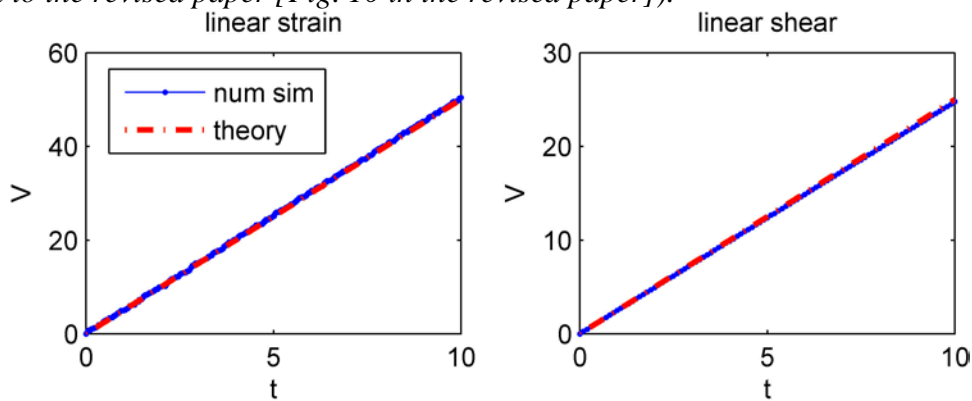


Figure 4. Comparison between numerically computed encounter volume (blue) and analytical predictions (eqs. (8) and (9)) (red) for the linear strain (left) and linear shear flows (right). For the linear shear flow $\alpha=0.1$, $R=5$, $dx=dy=R/25$; for the linear strain flow $\gamma=0.1$, $R=5$; $dx=dy=R/25$.

The analysis of the diffusive flow appears to be more complicated than we anticipated. Our analytical expression (1) did not check out against numerical simulations and was removed from the paper. The difficulty is that our original treatment of the diffusive model as a process where the distance from the initial position for all trajectories (rather than on average) grows as square root of time was too simplistic, whereas other available probability laws and trends based on diffusive model do not account for the fact that we count only first encounters. Our simulations indicate growth of the encounter number in proportion to some power γ of time, where γ is in the range .64 to .78. But we are unable to predict the value of γ and have instead just quoted the range γ obtained. We have also described some of the initial steps that need to be taken towards resolution of the problem and we hope that some reader might be able to draw on this to make further progress. All of this appears in the first several paragraphs of Section III.

9. Lines 310–311: “... vector flux of the scalar of interest. This linkage is made explicit by ...” This same concept of a net scalar flux (and corresponding trajectories) is in fact also adopted in studies on convective heat transfer and chemically-reacting flows [1, 2, 3, 4, 5]. Please mention this for a stronger connection with similar research and literature.

We thank the reviewer for pointing out the references on the Lagrangian interpretation of thermal heat transfer. When we published our paper on the Lagrangian interpretation of scalar fluxes, we were unaware of this work. We have added the references as requested.

10. Line 324: “Although this lack of uniqueness may seem troublesome ...” This ambiguity is in fact resolved in [5] by attaching physical validity to such an additional vector instead of treating it as an arbitrary field (see also remark below).

See our response to #11

11. Lines 347–348: “... it is most convenient to make use of the flexibility in the definition of the tracer flux ...” This suggests that the method produces arbitrary results and its physical meaning therefore is questionable. However, this approach can in fact be provided with a sound physical basis using the approach following [5]. Key to this is that, given linear transport equations, a scalar field c governed by a transport equation of the form (10) admits expression as the difference between two other physically-meaningful scalar fields c_A and c_B , each governed by $\partial c_A / \partial t + \nabla \cdot \mathbf{F}_A = S_A, \partial c_B / \partial t + \nabla \cdot \mathbf{F}_B = S_B$, (1)

with $\mathbf{F}_{A,B}$ and $S_{A,B}$ the corresponding fluxes and source terms, respectively. In [5], $S_A = S_B = 0$ and \mathbf{F}_A and \mathbf{F}_B are diffusive flux and advective-diffusive flux, respectively, of the same initial condition $c_A(\mathbf{x}, 0) = c_B(\mathbf{x}, 0) = c_0(\mathbf{x})$. In the current manuscript, also $S_A = S_B = 0$ yet \mathbf{F}_A and \mathbf{F}_B now both are the advective flux (i.e. $\mathbf{F}_{A,B} = \mathbf{u}c_{A,B}$) of the *different* initial conditions $c_A(\mathbf{x}, 0) = c_{A0}$ and $c_B(\mathbf{x}, 0) = c_{B0}(\mathbf{x})$. Hence, both problems, though physically different, allow for treatment by the same concept. Transport of difference $c' = c_B - c_A$ is governed by $\partial c' / \partial t + \nabla \cdot \mathbf{F}' = S'$, $\mathbf{F}' = \mathbf{F}_B - \mathbf{F}_A$, $S' = S_B - S_A$, (2)

with here $S' = 0$ and $\mathbf{F}' = \mathbf{u}c' = \mathbf{u}(c_B - c_A)$ the flux of c' (i.e. the anomaly and its flux in line 348). Thus anomaly c' in fact concerns the scalar transport relative to a physical reference state c_A instead of some arbitrary state. Here the reference state happens to remain uniform in time due to the advective transport of a uniform initial condition, i.e. $c_A(\mathbf{x}, t) = c_A(\mathbf{x}, 0) = c_{A0}$, yet the approach holds equally for any non-uniform (evolving) state c_A (enabling its employment also for more complicated problems). Moreover, note that \mathbf{u} needn't be divergence-free. It is

recommended to modify the discussion in Sec. IV according to the above in order to eliminate the (incorrect) impression of a conceptual flaw in the method.

We have recast our treatment of the dye flux in the Bickley jet as suggested, following the Speetjens (2012) arguments. We specifically introduce two scalar flux equations, one for c and one for the reference value c_o , and take the difference. This is indeed a more systematic approach, but we are not completely convinced that the flux vector so obtained by this methodology is always unique, or necessarily most desirable. The purely diffusive reference state that Speetjens favors may not be the only reference state that a reasonable person might choose: there could be alternatives. And in our problem c_o is just a small (but arbitrary) value.

Minor technical issues and corrections

1. Figs. 2–4: specify the spacing of the initial parcel positions.
2. Line 153: pronounces ! pronounced
3. Line 231: the title of Sec. III is rather long and confusing. Please consider a more compact title.
4. Line 266: reference moving ! reference frame moving

[1] A. Bejan, Convection Heat Transfer, Wiley, New York (1995).

[2] V.A.F. Costa, Bejan’s heatlines and masslines for convection visualization and analysis, Appl. Mech. Rev. 59 (2006), 127.

[3] S. Mahmud, R. A. Fraser, Visualizing energy flows through energy streamlines and pathlines, Int. J. Heat Mass Transfer 50 (2007), 3990.

[4] A. Mukhopadhyay, X. Qin, S. K. Aggarwal, I. K. Puri, On extension of “heatline” and “massline” concepts to reacting flows through use of conserved scalars, ASME J. Heat Transfer 124 (2002), 791.

[5] M. F. M. Speetjens, A generalised Lagrangian formalism for thermal analysis of laminar convective heat transfer, Int. J. Therm. Sci. 61 (2012), 79.

Reference state c_o [5] e.g. corresponds with the non-uniform and unsteady temperature field due to diffusive heat transfer only; c_o is the contribution to the total advective-diffusive temperature field c due to the flow u . e. $c_o = 0$ only if $u = 0$ and thus captures the thermal transport that is effectively induced by the fluid motion.

All the minor technical corrections have been made, and all new references added to the revised paper.

Interactive comment on “Trajectory encounter number as a diagnostic of mixing potential in fluid flows” by Irina I. Rypina and Larry J. Pratt

Anonymous Referee #2

Received and published: 2 January 2017

In this paper the authors introduce a new Lagrangian descriptor to give a measure of the effectiveness of a flow to mix over a finite time. The idea is to start with a finite grid of K initial trajectories, and, for each trajectory compute the number other trajectories that come within a radius R of the given one, thus they compute

$$N(x^c; R, T; K) = \sum_{k=1}^K I(\min_{s \in [0, T]} (\| \curvearrowright_s(x_k) - \curvearrowright_t(x) \|) \leq R) \square$$

where we define the indicator function I to return 1 if true and 0 if false, and the flow $\curvearrowright_t(y) = x(t; y)$ for an initial point y . (The authors never give such a formula, and ignore the dependence on the grid).

While this is an intriguing idea, it is not clear how to make it mathematically well-defined. It seems to have some relation to finite time entropy, as introduced in the reference by Froyland as this computes the growth rate of number of distinguishable trajectories. Would it be better to talk about a growth-rate here too? I feel that one should not just compute something that is so specific to choices, but first make a consistent mathematical definition: something that exists in the limit as the grid of initial points becomes infinitely fine, say, and then compute it, showing that the computations are, to some approximation, giving the desired quantity.

Following the reviewer’s suggestion, we reformulated the mixing potential concept in terms of the trajectory encounter mass, M , and its simplified approximation – the encounter volume, V , which we now define in a continuous limit of infinitely many infinitesimally small water parcels or, equivalently, an infinitely dense grid of initial positions. For an incompressible flow densely seeded with particles, the encounter volume V can be approximated by $V \cong N\delta V$, where N is the encounter number, i.e., the number of trajectories passing through an encounter sphere of radius R moving with the parcel over time T , and δV is a parcel volume element. We have also included a mathematical expression for the encounter number as the reviewer suggested above. The beginning of Sec I(b) of the revised paper now reads:

“For a given reference trajectory, $\vec{x}(\vec{x}_0, t_0; T)$, the *encounter mass*, $M(\vec{x}_0, t_0; T)$, is defined as the total mass of fluid that passes within a radius R of reference trajectory over a finite time interval $t_0 < t < t_0 + T$. One might imagine a sphere that has radius R and that is centered at and moves with the reference trajectory. The encounter mass then consists of the mass of the fluid that is initially located within the sphere along with the mass of all the fluid that passes through the sphere over the time interval $t_0 < t < t_0 + T$. Note that it is generally not possible to compute the latter by simply integrating the mass flux into the sphere over $t_0 < t < t_0 + T$ since some fluid may leave and then re-enter the sphere and would be counted more than once, so Lagrangian information is required to keep track of the history of each fluid parcel trajectory entering the sphere.

To this end, subdivide the entire fluid at $t = t_0$ into small compact fluid elements with masses $\delta M_i = \rho_i \delta V_i$, where ρ_i is the density of a fluid element and δV_i is its volume. We wish to follow the motion of each fluid element over time interval $t_0 < t < t_0 + T$, and we assume that the

elements remain compact over such time, so that the motion of each fluid element can be well-represented by one trajectory. If the fluid elements stretch and deform too much, we can evoke the continuum hypothesis and make δM sufficiently small that such compactness is assured. In the limit of infinitesimal fluid elements, $\delta M_i \rightarrow dM$, we can associate with each infinitesimal fluid element a unique trajectory. The encounter mass is then

$$M = \lim_{dM_i \rightarrow 0} \sum_i dM_i.$$

For an incompressible flow, the density and volume of each fluid element, ρ_i and δV_i , remain constant following a trajectory, although different fluid elements are still allowed to have different densities such as, for example, in stratified 3D geophysical flows. If the flow is unstratified, the densities of all fluid elements are equal, $\rho_i = \rho$, and the encounter mass becomes

$$M = \rho V,$$

where

$$V(\vec{x}_0, t_0; T) = \lim_{dV_i \rightarrow 0} \sum_i dV_i$$

is the *encounter volume* – the total volume of fluid that passes within a radius R of reference trajectory over a finite time interval $t_0 < t < t_0 + T$. When all volume elements are equal, $dV_i = dV$, the encounter volume can be further simplified to

$$V = \lim_{dV \rightarrow 0} N dV,$$

where the *encounter number*, $N(\vec{x}_0, t_0; T)$, is the number of trajectories that come within a radius R of the reference trajectory over a time interval $t_0 < t < t_0 + T$. We will refer to t_0 as the starting time, T as the trajectory integration time, and \vec{x}_0 as the trajectory initial position, i.e., $\vec{x}(\vec{x}_0, t_0; T = 0) = \vec{x}_0$. For practical applications with geophysical flows, the limit in the definition of the encounter volume can be dropped and one can simply use the approximation

$$V \approx N \delta V$$

with the dense grid of initial positions \vec{x}_0 . Mathematically, the encounter number can be written as $N = \sum_{k=1}^K \mathbb{I}(\min(|\vec{x}_k(\vec{x}_0, t_0; T) - \vec{x}(\vec{x}_0, t_0; T)|) \leq R)$ where the indicator function \mathbb{I} is 1 if true and 0 if false, and K is the total number of Lagrangian particles released. The encounter volume depends on the starting time, integration time, encounter radius, and the number of trajectories (i.e., grid spacing); all of these parameter dependences will be discussed below. Once the encounter volume is estimated, regions of space with large/small V would then be associated with enhanced/inhibited mixing potential."

1. The authors fix the grid size and do not investigate how the number depends on grid size. They do not even tell the reader what grids are used in the first two examples!

We apologize for not providing the grid size that we used in the first two examples. This info has been included in the revision.

In the revised paper, we also present a set of new numerical simulations exploring the dependence of the encounter volume on grid size. The following paragraph discussing this issue has been added to the revision at the end of Sec II(a):

“We have carried out numerical simulations (Fig. 6 [Fig. 5 here]) to investigate the dependence of the encounter volume on the grid size, and to come up with a rule of thumb recommendation regarding the appropriate grid spacing. Our simulations suggest that the encounter volume values (approximated by $V \approx N \delta V$) are relatively insensitive to the variations of grid spacing between 1/10 and 1/2 of the encounter radius (with the encounter radius being a fraction of the size of the feature of interest, as suggested by Fig. 2), and that the major effect of a coarser grid is the degraded resolution of the resulting V map, rather than incorrect V values.”

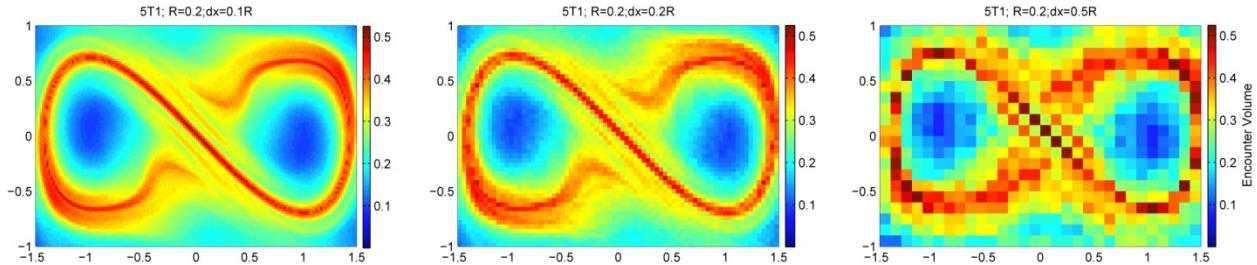


Figure 5. Encounter volume, V , for the Duffing Oscillator flow for various grids of initial positions, from dense grid spacing of 0.02 (left), to intermediate grid spacing of 0.04 (middle), to coarse grid spacing of 0.1 (right). Encounter radius, $R=0.2$, and integration time, $T=6.67$, are the same in all 3 simulations.

2. It seems like it would be better to define something that (like they mention in the conclusions) represents a “fraction” or “density” of encounters. Mathematically one would probably define something that uses an \sim construction: Given trajectories on an \sim grid, how many get closer than \sim ? Then take limits. if possible, of a density or growth-rate?

As explained above, we now quantify mixing potential using the encounter volume, V , instead of the encounter number. The encounter radius, which defines how close to each other two parcels need to be in order to be counted as an encounter, is kept finite and treated as a parameter. The dependence of V on R is investigated numerically, and analytical arguments are presented that relate V , R and grid spacing to the size of the features of interest, all in agreement with numerical simulations.

3. Another possible quantity, though instead of measuring “mixing” would be one that measures “ergodicity”: How many grid cells does a given trajectory cover? This might also be an interesting quantity, and much easier to compute. Note that mixing is equivalent to each trajectory visiting every grid cell.

The relationship between Lagrangian Coherent Structures and ergodicity has been explored in our prior work, please see the following paper for the discussion of this topic: Rypina, I. I., S.

Scott, L. J. Pratt, and M. G. Brown (2011). *Investigating the connection between complexity of isolated trajectories and Lagrangian coherent structures*. *Nonlin. Proc. Geophys.*, **18**, 977-987, doi:10.5194. This reference has been added to the revised paper.

4. The authors do not really compare their results with any of the other many possible descriptors like FTLE, or perhaps more relevantly the finite time entropy.

At the end of Sec II(a) of the revised paper, we added a comparison between encounter volume V and FTLEs, along with a discussion of the advantages and limitations of both methods.

“With a variety of dynamical systems techniques available, it is important to understand the advantages and limitation of the different methods. We compared the encounter volume to two well-established and commonly-used methods, the Poincare section (Fig. 3) and the FTLEs (Fig. 5 [Fig. 6 here]). Since the Poincare section requires stroboscopic sampling of trajectories in time, it can only be applied to time-periodic flows, and requires that trajectories are computed over long integration time, typically thousands of the periods of the perturbation. On the other hand, it generally requires only a few parcels to be released at some key locations, rather than releasing a dense grid of initial positions, to map out the entire phase space. The encounter volume and FTLEs, on the other hand, are not limited to time-periodic flows, and also work with significantly shorter segments of trajectories (longest integration time in our simulations in Fig. 2 is only 50 periods of perturbation). They are also better suited for identifying manifolds than the Poincare sectioning as they do not require any *a priori* knowledge about the location of the hyperbolic trajectory. On the other hand, they require many more parcels to be released in order to map out the phase space. When applied to the same set of trajectories (same initial positions and integration times), the FTLEs and the encounter volume methods produced similar results (Fig. 5), with V being arguably better suited for 1) identifying the coherent core regions of eddies, where FTLEs have spiraling patterns that complicate the analysis, and 2) producing more continuous segments of manifolds at intermediate integration times, when FTLE-based ridges get discontinuous near the turning points of a manifold. The advantage of FTLEs, on the other hand, is that they have fewer parameters (T and grid spacing), whereas V also depends on R , and that they less expensive computationally. The more expensive computational cost of V compared to FTLEs is due to two reasons: first, the FTLEs only depend on the initial and final positions of trajectories, whereas V depends on the entire trajectory history; and second, FTLEs depend on the relative distance between a trajectory and its closest neighbors, whereas V keeps tracks of encounters with all trajectories, not just the neighboring trajectories. Thus, the cost of evaluating FTLE for each particle is independent of the total number of particles released, and the cost of evaluating V for each particle increases in proportion to the number of particles (since one needs to keep track of encounters with all particles). The calculation of V is still feasible for realistic geophysical flows, as is illustrated below. Note also that, depending on the physical question being studied, the information about the entire trajectory, not just the final and initial position, might in fact be advantageous.”

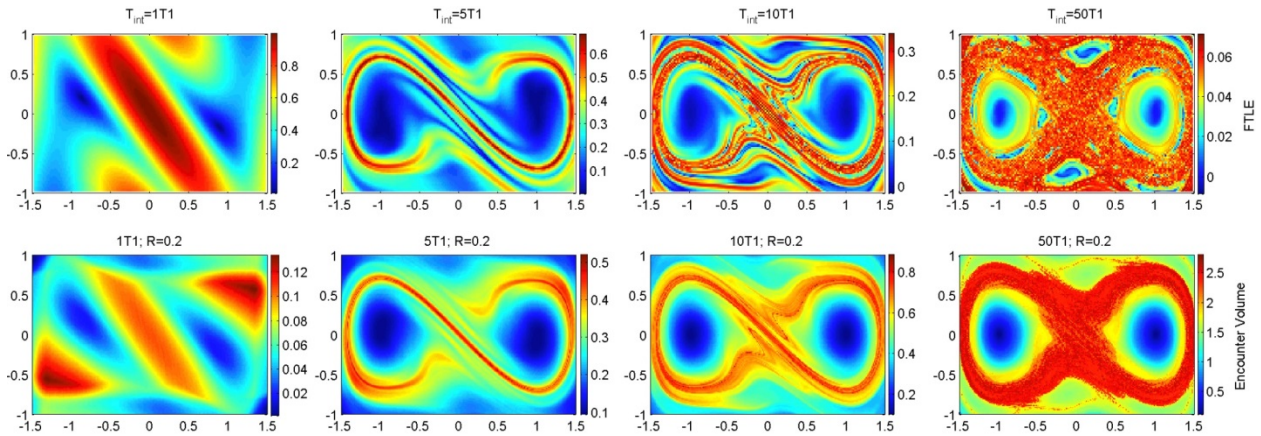


Figure 6. Comparison between the FTLEs (top) and the encounter volume (bottom; same as middle row of Fig. 2) for the Duffing Oscillator flow for various integration times, from $T=0.1T_{\text{pert}}=0.13$ (on the left) to $T=50T_{\text{pert}}=66.67$ (on the right). The same set of trajectories, deployed on a dense initial grid with 0.02 grid spacing is used in all simulations. In the bottom panels, $R=0.2$.

- The authors do not discuss the complexity of this computation. It seems to me that it is much more computationally intensive than, e.g., the FTLE, which does not involve comparing all distances between all trajectories. It is this really a feasible calculation? How does it scale with the number of trajectories and the time?

We have added a discussion of the complexity of the calculation and scaling with the number of trajectories. The reviewer is certainly correct that the encounter volume diagnostic is more computationally expensive than FTLEs. However, the calculation of the encounter volume is certainly feasible for realistic oceanic flows, as illustrated in our data-based example #3 (satellite-based geostrophic velocities). Please see our answer to comment 4 above.

- The authors do some basic investigation of how N depends upon R and t , but the computations of N for the simple diffusive and shear cases seem wrong to me: In particular, if we take a planar diffusive process with diffusion coefficient D , and make the assumption (not clear to me) that one can transform to a frame moving with one particle (doesn't this double the diffusivity?), ...

We thank the reviewer for pointing out that the diffusivity is doubled in the reference frame moving with a particle. This has been corrected in the revised paper.

...then one should compute the probability of a particle finding itself inside a disk of radius R for any time $0 < t < T$, given it starts at some point (x_0, y_0) in the plane. For example for the process on the line, then at a FIXED time t this means evaluating the integral

$$P(\clubsuit x(t) \clubsuit < R \clubsuit x(0) = x_0) = \frac{1}{\sqrt{2Dt}} \int_{-R}^R \exp\left[-\frac{(x-x_0)^2}{2Dt}\right] dx$$

which can be evaluated in terms of error functions. The authors seem to assume a deterministic motion with the root mean square distance, which seems to me to be wrong.

We did not assume a deterministic motion, but our treatment of the diffusive motion was indeed incorrect and our analytical expression (1) disagreed with numerical simulations. We have removed expression (1) from the revised paper. Also see our response to comment #8 of the first reviewer.

They also ignore particles that start inside the circle of radius R (not so important if they want a large t limit I suppose).

The reviewer is correct; we did not include the volume of the encounter sphere (or the area of the encounter circle in our 2d examples) in our encounter volume calculations/formulas. We have clarified this in the revised paper, and noted that “To include the volume of fluid that is initially located within the encounter sphere (or within the encounter circle in this 2D case), one needs to add πR^2 to expression (2). The contribution of this term gets negligibly small as $T \rightarrow \infty$.”

Now to compute N you have to sum (or integrate?) this probability over an initial distribution of initial points, say x_0 is uniform on a box, perhaps? And you have to somehow compute the probability over all times $0 < t < T$. This calculation seems very different from the one given in the paper.

The formula for the pdf of a particle position that the reviewer wrote above does not take into account that we are interested in first encounters, not all encounters. In the revised paper, we have outlined some initial steps towards deriving the connection between V and diffusivity along the lines suggested by the reviewer, but we have not been able to follow through with this derivation; this is left for a future study.

The shear flow is easier, but I think not done correctly either. One has to compute the area of the region that sweeps into the circle of radius R , but also include the particles that start inside the disk.

Again, the reviewer is correct; our expression did not include the area of the encounter sphere, πR^2 . We have added a note on this similar to the one for the strain flow.

While this paper has an intriguing idea, I think it needs substantial revision and correction before publication.

We are glad that the reviewer found our ideas intriguing, and we hope that we addressed all of the reviewer’s concerns in the revised paper.

Interactive comment on “Trajectory encounter number as a diagnostic of mixing potential in fluid flows” by Irina I. Rypina and Larry J. Pratt

Dr Koshel

kvkoshel@poi.dvo.ru

Received and published: 19 January 2017

It is only the short comment, not deep review. We can see many finite time Lagrangian descriptors suggested last time, maybe 20 or 30 years. For example, the Poincare section is calculated for finite time. Most descriptors follow from dynamical systems theory constructions. It well discussed in reviewers comments. I have an analogous question. Is it possible to make some connection between the encounter number and the Poincare recurrence. In any case, I think, the most Lagrangian descriptors used, for example, in oceanography have no strong mathematical foundation, but very useful for data analyze and interpretation. I also think the descriptor suggested here is more expensive in comparison with FLTE or some other. But it seems, it has some advantage in physical interpretation. I think the manuscript is suitable for publication in Nonlinear Processes in Geophysics, after some revision.

A discussion of the differences and similarities between the encounter volume and the Poincare section methods have been added to the revised manuscript. We also added a discussion of the computational cost of the calculation, and a comparison with FTLEs. The new text at the end of Sec. II(a) now reads:

“With a variety of dynamical systems techniques available, it is important to understand the advantages and limitation of the different methods. We compared the encounter volume to two well-established and commonly-used methods, the Poincare section (Fig. 3) and the FTLEs (Fig. 5). Since the Poincare section requires stroboscopic sampling of trajectories in time, it can only be applied to time-periodic flows, and requires that trajectories are computed over long integration time, typically thousands of the periods of the perturbation. On the other hand, it generally requires only a few parcels to be released at some key locations, rather than releasing a dense grid of initial positions, to map out the entire phase space. The encounter volume and FTLEs, on the other hand, are not limited to time-periodic flows, and also work with significantly shorter segments of trajectories (longest integration time in our simulations in Fig. 2 is only 50 periods of perturbation). They are also better suited for identifying manifolds than the Poincare sectioning as they do not require any *a priori* knowledge about the location of the hyperbolic trajectory. On the other hand, they require many more parcels to be released in order to map out the phase space. When applied to the same set of trajectories (same initial positions and integration times), the FTLEs and the encounter volume methods produced similar results (Fig. 5), with V being arguably better suited for 1) identifying the coherent core regions of eddies, where FTLEs have spiraling patterns that complicate the analysis, and 2) producing more continuous segments of manifolds at intermediate integration times, when FTLE-based ridges get discontinuous near the turning points of a manifold. The advantage of FTLEs, on the other hand, is that they have fewer parameters (T and grid spacing), whereas V also depends on R , and that

they less expensive computationally. The more expensive computational cost of V compared to FTLEs is due to two reasons: first, the FTLEs only depend on the initial and final positions of trajectories, whereas V depends on the entire trajectory history; and second, FTLEs depend on the relative distance between a trajectory and its closest neighbors, whereas V keeps tracks of encounters with all trajectories, not just the neighboring trajectories. Thus, the cost of evaluating FTLE for each particle is independent of the total number of particles released, and the cost of evaluating V for each particle increases in proportion to the number of particles (since one needs to keep track of encounters with all particles). The calculation of V is still feasible for realistic geophysical flows, as is illustrated below. Note also that, depending on the physical question being studied, the information about the entire trajectory, not just the final and initial position, might in fact be advantageous.”

I can find few misprints in the manuscript which not mentioned by reviewers.

We have carefully checked the revised manuscript for the misprints and typos.

Minor technical issues and correction lines 336,371-373 t_0 is used and may be better to use t_0
Caption to figure 8: U-star and Nstar are used. Maybe it will be better to use U_{v_0} and N_{v_0}

We have changed t_0 to t_0 , but changed Ustar and Nstar to u^ and N^* .*

Trajectory encounter volume as a diagnostic of mixing potential in fluid flows

Irina I. Rypina¹ and Larry J. Pratt¹

¹ Woods Hole Oceanographic Institution, Physical Oceanography department,
266 Woods Hole rd., Woods Hole MA, 02543

Corresponding author email: irypina@whoi.edu

Abstract

Fluid parcels can exchange water properties when coming in contact with each other, leading to mixing. The trajectory encounter mass and a related simplified quantity, encounter volume, are introduced as a measure of the mixing potential of a flow. Encounter volume quantifies the volume of fluid that passes close to a reference trajectory over a finite time interval. Regions characterized by low encounter volume, such as cores of coherent eddies, have low mixing potential, whereas turbulent or chaotic regions characterized by large encounter volume have high mixing potential. The encounter volume diagnostic is used to characterize mixing potential in 3 flows of increasing complexity: the Duffing Oscillator, the Bickley Jet, and the altimetry-based velocity in the Gulf Stream Extension region. An additional example is presented in which the encounter volume is combined with the u^* -approach of Pratt et al., 2016 to characterize the mixing potential for a specific tracer distribution in the Bickley Jet flow. Analytical relationships are derived connecting encounter volume to shear and strain rates for linear shear and linear strain flows, respectively. It is shown that in both flows the encounter volume is proportional to time.

I. Encounter volume

a. main idea

Mixing is an irreversible exchange of properties between different water masses. This process is important for maintaining the oceanic large-scale stratification and general circulation, and it plays a key role in the redistribution of bio-geo-chemical tracers throughout the world oceans. Mixing occurs between different water masses when they come in direct contact with each other. Thus, mixing potential of the flow, i.e., the opportunity for mixing to occur, is generally enhanced in regions where water parcels meet or encounter many other water parcels and thus are exposed to a large amount of fluid passing by them as the flow evolves. This would be the case, for example, for a parcel within a chaotic zone –a region of the flow that is in a state of chaotic advection. There, the separation between initially nearby water parcels grows exponentially in time and, in the infinite time limit, each water parcel encounters all the other water parcels within the same zone and gets in contact with the entire volume of the chaotic zone. Similarly, high encounter volumes will exist in turbulent regions. In contrast, mixing potential and encounter volume is expected to be smaller in regions where water parcels do not experience many encounters with other water parcels and remain close to their initial neighbors

37 as the flow evolves. This would be the case, for example, for a water parcel that is located inside
38 a coherent eddy. If the eddy is in a state of solid body rotation, the water parcel would forever
39 stay close to its initial neighbors and will not have any new encounters at all. If some amount of
40 azimuthal shear is present within the eddy, then for a water parcel located at a radius r from the
41 eddy center, encounters will be limited to those water parcels located within a circular strip
42 centered at the same r .

43 Of course, the presence of a mixing potential does not guarantee that the mixing of a tracer will
44 occur: it is also essential that the tracer distribution is non-uniform, so that irreversible property
45 exchange can take place between different water parcels during their encounters. This exchange
46 happens by diffusion and therefore relies on a concentration difference between two parcels.
47 Thus, the intensity of mixing would depend on both the tracer distribution and the flow, whereas
48 mixing potential is the property of only the flow field alone. In this work we introduce the
49 concept of an *encounter mass*, M , and *encounter volume*, V , which serves as a simplified
50 representation of M in incompressible flows, as an objective measures of encounters between
51 different fluid elements in order to quantify the mixing potential of a fluid flow. There are many
52 existing trajectory-based measures of fluid stirring; ours has the virtue of having a
53 straightforward physical interpretation and being easy to implement and immediately applicable
54 to ocean float and drifter data. Our method does not require sophisticated book keeping as in
55 braided theory (Allshouse and Thiffeault, 2012) or finite-time entropy (Froyland and Padberg-
56 Gehle, 2012).

57 b. definition and numerical implementation

58 For a given reference trajectory, $\vec{x}(\vec{x}_0, t_0; T)$, the *encounter mass*, $M(\vec{x}_0, t_0; T)$, is defined as the
59 total mass of fluid that passes within a radius R of reference trajectory over a finite time interval
60 $t_0 < t < t_0 + T$. One might imagine a sphere that has radius R and that is centered at and moves
61 with the reference trajectory. The encounter mass then consists of the mass of the fluid that is
62 initially located within the sphere along with the mass of all the fluid that passes through the
63 sphere over the time interval $t_0 < t < t_0 + T$. Note that it is generally not possible to compute
64 the latter by simply integrating the mass flux into the sphere over $t_0 < t < t_0 + T$ since some
65 fluid may leave and then re-enter the sphere and would be counted more than once, so
66 Lagrangian information is required to keep track of the history of each fluid parcel trajectory
67 entering the sphere.

68
69 To this end, subdivide the entire fluid at $t = t_0$ into small compact fluid elements with masses
70 $\delta M_i = \rho_i \delta V_i$, where ρ_i is the density of a fluid element and δV_i is its volume. We wish to follow
71 the motion of each fluid element over time interval $t_0 < t < t_0 + T$, and we assume that the
72 elements remain compact over such time, so that the motion of each fluid element can be well-
73 represented by one trajectory. If the fluid elements stretch and deform too much, we can evoke
74 the continuum hypothesis and make δM sufficiently small that such compactness is assured. In

75 the limit of infinitesimal fluid elements, $\delta M_i \rightarrow dM$, we can associate with each infinitesimal fluid
 76 element a unique trajectory. The encounter mass is then

$$77 \quad M = \lim_{dM_i \rightarrow 0} \sum_i dM_i.$$

78 For an incompressible flow, the density and volume of each fluid element, ρ_i and δV_i , remain
 79 constant following a trajectory, although different fluid elements are still allowed to have
 80 different densities such as, for example, in stratified 3D geophysical flows. If the flow is
 81 unstratified, the densities of all fluid elements are equal, $\rho_i = \rho$, and the encounter mass
 82 becomes

$$83 \quad M = \rho V,$$

84 where

$$V(\vec{x}_0, t_0; T) = \lim_{dV_i \rightarrow 0} \sum_i dV_i$$

85 is the *encounter volume* – the total volume of fluid that passes within a radius R of reference
 86 trajectory over a finite time interval $t_0 < t < t_0 + T$. When all volume elements are equal,
 87 $dV_i = dV$, the encounter volume can be further simplified to

$$88 \quad V = \lim_{dV \rightarrow 0} N dV,$$

89 where the *encounter number*, $N(\vec{x}_0, t_0; T)$, is the number of trajectories that come within a radius
 90 R of the reference trajectory over a time interval $t_0 < t < t_0 + T$. We will refer to t_0 as the
 91 starting time, T as the trajectory integration time, and \vec{x}_0 as the trajectory initial position, i.e.,
 92 $\vec{x}(\vec{x}_0, t_0; T = 0) = \vec{x}_0$. For practical applications with geophysical flows, the limit in the
 93 definition of the encounter volume can be dropped and one can simply use the approximation

$$V \approx N \delta V$$

94 with the dense grid of initial positions \vec{x}_0 . Mathematically, the encounter number can be written
 95 as $N = \sum_{k=1}^K \mathbb{I}(\min(|\vec{x}_k(\vec{x}_0, t_0; T) - \vec{x}(\vec{x}_0, t_0; T)|) \leq R)$ where the indicator function \mathbb{I} is 1 if true
 96 and 0 if false, and K is the total number of Lagrangian particles released. The encounter volume
 97 depends on the starting time, integration time, encounter radius, and the number of trajectories
 98 (i.e., grid spacing); all of these parameter dependences will be discussed below. Once the
 99 encounter volume is estimated, regions of space with large/small V would then be associated
 100 with enhanced/inhibited mixing potential. For the remainder of this paper, we will focus on
 101 incompressible fluid flows and will be concerned with the encounter volume, rather than
 102 encounter mass.

103

104 We define $V(\vec{x}_0, t_0; T)$ and $N(\vec{x}_0, t_0; T)$ based on the number of encounters with different
105 trajectories, not the total number of encounter events, so even if some trajectory first comes close
106 to the reference trajectory, then moves away and then re-approaches it again later, it is only
107 counted once. In a flow field with no sources or sinks of tracer variance, where variance is
108 therefore decaying, it is reasonable to expect that most property exchange between two parcels
109 will often occur during their first encounter, thus the motive for counting only the first encounter.
110 Note that this assumption may not hold if the parcels re-acquire different properties after their
111 first encounter due to encountering and exchanging properties with other parcels. In this case, or
112 in the case when tracer variance is being continuously introduced, it may be more reasonable to
113 count the total number of encounters.

114 For a numerical implementation of the trajectory encounter volume-based mixing
115 characterization, one would need to start, at some time t_0 , with a grid of initial positions
116 spanning the flow domain, and then evolve trajectories under the flow field over the time interval
117 T . This time interval should be chosen based on the physical properties of the flow and with
118 specific scientific questions in mind. For example, if the research focus is on ocean submesoscale
119 dynamics, the time scale T would be on the order of hours to days, whereas the corresponding
120 time scale for mesoscale dynamics would be on the order of weeks to months.

121 $V(\vec{x}_0, t_0; T)$ is a Lagrangian quantity that characterizes mixing potential of a flow over a time
122 interval from t_0 to $t_0 + T$. As the flow field evolves in time, its mixing characteristics can
123 change and $V(\vec{x}_0, t_0; T)$ will reflect this change. For example, if a coherent eddy with weak
124 mixing potential, embedded in a chaotic zone with enhanced mixing potential, was present in the
125 flow from time t_1 to time t_2 , but it dispersed and disappeared afterwards, then $V(\vec{x}_0, t_0; T)$ is
126 expected to be small at those locations \vec{x}_0 that correspond to the interior of an eddy for $t_0 \geq t_1$
127 and $t_0 + T \leq t_2$, whereas for $t_0 > t_2$, when the eddy is no longer present, $V(\vec{x}_0, t_0; T)$ would
128 increase. Dependences on T and t_0 are similarly expected to be present within a chaotic zone.

129 In the infinite time limit, $T \rightarrow \infty$, when all parcels within a chaotic zone (or turbulent region) of
130 finite extent encounter all other parcels within the same chaotic zone, the encounter volume
131 $V(\vec{x}_0, t_0; T \rightarrow \infty)$ approaches a constant equal to the volume (or area in 2d) of the chaotic zone.
132 For 2D, incompressible flow, the encounter rates over finite T are locally the largest near a
133 hyperbolic trajectory and along the segments of its associated stable manifolds. The stable
134 manifolds serve as pathways that bring water parcels from remote regions into the vicinity of the
135 hyperbolic trajectory, where parcels stay for extended periods of time, and where many
136 encounters occur. Note that the unstable manifolds, on the other hand, will rapidly remove a
137 particle from a hyperbolic region, thus limiting its exposure to the high-encounter region near the
138 hyperbolic trajectory. For this reason, the unstable manifolds are not revealed by encounter
139 volume calculation performed in forward time and require a backward-time calculation instead.
140 This exclusive link between forward/backward in time calculation of trajectories and
141 stable/unstable manifolds, respectively, is not specific to the encounter volume diagnostic, but

142 rather is typical for many finite-time methods from the dynamical systems theory, including
143 finite-time Lyapunov exponents (FTLEs), which in forward time approximate segments of stable
144 manifold as maximizing ridges (Haller, 2002; Shadden et al., 2005; Lekien and Ross, 2010).

145 Since locations of hyperbolic trajectories and manifolds generally evolve in time, $V(\vec{x}_0, t_0; T)$ is
146 expected to also vary with t_0 . As the trajectory integration time T increases, water parcels
147 initially located further from the hyperbolic trajectory will have the opportunity to come into its
148 vicinity along the stable manifold. Such parcels, as they approach the hyperbolic trajectory, are
149 expected to have more encounters than their neighbors that are initially located off the manifold
150 and thus bypass the vicinity of the hyperbolic trajectory where many encounters occur. Thus,
151 $V(\vec{x}_0, t_0; T)$ reveals longer segments of stable manifolds for longer integration time T , as will be
152 illustrated numerically in the next section. In the long integration time limit, when each
153 manifold, either stable or unstable, densely fills the entire chaotic zone forming a dense
154 homoclinic or heteroclinic tangle, the whole tangle will be characterized by high encounter
155 volumes in both forward and backward time. Again, this is similar to how the maximizing ridges
156 of the forward time FTLEs elongate and sharpen with increasing integration time.

157
158 The radius R , which defines how close to a reference trajectory should another trajectory come in
159 order to be counted as an encounter, is an important parameter for the calculation of the
160 encounter volume V . Generally, R should be small compared to the spatial scale of the smallest
161 features of interest. Specifically, for the V field to delineate a flow feature, say, an eddy,
162 trajectories within the eddy interior should not encounter those on its exterior. The boundary
163 region near the eddy perimeter, where such encounters can occur, has the width $2R$. So, if that
164 width is comparable to or larger than the eddy size, then the eddy would get completely smeared
165 out and will not be resolved. From a practical viewpoint, however, using very small R would
166 require very dense grids of trajectories to be computed, otherwise zero or very small number of
167 trajectory encounters will occur in the entire flow domain. Numerical examples in the next
168 section suggest that choosing R to be a fraction, up to about half of the size of the smallest
169 features of interest work best.

170 Finally, the approximation $V \approx N \delta V$ breaks down for sparse grids of initial positions with the
171 insufficient number of Lagrangian particles, when N is small and δV is large. It also works
172 poorly when applied to 2D divergent flows due to δV changing following trajectories. Numerical
173 simulations in the next section suggest that grid spacing $\leq R/2$ is sufficient, and that the method
174 can also be applied to characterize mixing potential in slightly divergent two-dimensional flows.

175 Once the time scale T is identified, grid of initial positions is chosen, trajectories are computed,
176 radius R is defined, and the number of encounters, $N(\vec{x}_0, t_0; t)$, is counted for each trajectory,
177 then the encounter volume can be estimated as $V \approx N \delta V$ and plotted as a function of the
178 trajectory initial position \vec{x}_0 . The resulting V field delineates the flow regions with different
179 mixing properties as subdomains having different values of V .

180 II. Examples

181 We proceed to test the performance of the encounter volume technique in quantifying mixing
182 potential for several geophysically relevant sample flows of increasing complexity, starting from
183 a simple analytically prescribed periodically perturbed double-gyre Duffing Oscillator system,
184 followed by a dynamically consistent solution of the PV conservation equation on a beta-plane
185 known as the Bickley Jet, and finishing with an observationally based geostrophic velocity field
186 in the North Atlantic derived from the sea surface height altimetry.

187 a. Duffing Oscillator

188 The Duffing Oscillator flow and its figure-eight geometry has become a standard test case for
189 emerging techniques related to the dynamical systems theory. This flow consists of two gyres
190 with the same sign of rotation (clockwise in our case), whose elliptic centers oscillate in time
191 around their mean position. A hyperbolic point is located at the origin between the two gyres,
192 and a pair of stable and unstable manifolds emanate from it forming a figure eight in the absence
193 of the time dependent perturbation, or forming a classic homoclinic tangle in the presence of the
194 perturbation. The velocity field is two-dimensional and incompressible and is given by $u = y$
195 and $v = (x - ax^3)(1 + \epsilon \cos(\omega t + \phi))$ with $a = 1$, $\omega = 3\pi/2$, $\phi = \pi/4$ and $\epsilon = 0.1$. With
196 these parameters, the Poincare section (Fig. 1 bottom) shows the presence of two main regular
197 elliptic regions with $O(1)$ radius corresponding to the interiors of the gyres, which are embedded
198 into a figure-eight shaped chaotic zone, within which a number of island chains with smaller
199 regular islands are present. The winding time for most trajectories in the system is on the order of
200 $5T_{pert}$ with $T_{pert} = \frac{2\pi}{\omega}$, except for trajectories near the hyperbolic point for which winding time
201 is much longer (Fig. 1 top).

202 The encounter volume was computed for a range of trajectory integration times, from $T = T_{pert}$
203 (which is significantly shorter than trajectory winding time) to $T = 50T_{pert}$ (significantly longer
204 than trajectory winding time), and for a range of encounter radii, from $R = 0.01 \ll R_{eddy}$
205 (significantly smaller than the eddy core radius) to $R = 1 \approx R_{eddy}$ (comparable to the eddy core
206 radius). The results in Fig. 2 suggest that the encounter volume method works best for
207 integration times longer than the trajectory winding time and encounter radius about 1/3 to 1/2 of
208 the gyre radius (right 3 panels of the middle row). For very small encounter radius (top row), V
209 is noisy because trajectories simply do not encounter many neighbors. Thus, delineating the
210 domain into regions with different mixing potential, as in the top right panel, requires long
211 integration time. For $T = 50T_{pert}$, good agreement with the Poincare section is observed, and
212 the use of small encounter radius allows for a precise identification of smaller regular island
213 chains, such as the chains of 4 islands located just outside of the perimeter of both left and right
214 eddy cores. Note that the noise in the V field can be suppressed by using a denser initial grid of
215 trajectories, but at the cost of a more expensive computation. For very short integration times
216 (left column) when trajectory segments are very short, the encounter volume is not capturing the

217 difference between the regular and chaotic regions. This is not surprising as velocity shear is
218 probably a dominating factor over such small times. As the integration time increases, the
219 difference in encounter volume becomes more pronounced between trajectories that remain
220 within the eddy cores and trajectories that are free to move around the chaotic zone. Over a time
221 scale of approximately one winding period (or about 5 periods of the perturbation; second
222 column), the two regular eddy cores (blue regions with small V) and a segment of the stable
223 manifold (red curve emanating from the origin with largest V) becomes clearly visible for $R=0.2$
224 and $R=1$. The revealed manifold segment becomes longer, narrower and more tangled,
225 eventually filling up the whole chaotic zone. At the same time, the shape of the core region
226 becomes more exact and approaches the “true” core in the Poincare section as the integration
227 time increases to 50 periods of the perturbation. The agreement with Poincare section is excellent
228 in the right middle panel, although the smaller island chains are not as visible as in the top right
229 panel because of the use of a larger encounter radius that is comparable to their size (see Fig. 3).
230 Finally, for the large encounter radius that is comparable to the size of the eddy (bottom row),
231 the boundary region near perimeter of an eddy, within which trajectories on the inside of the
232 eddy can encounter trajectories passing by on the outside, is as wide as the eddy itself, essentially
233 wiping out all small scales from the V field. All of these trends are in agreement with theoretical
234 expectations described in Section I.

235
236 In order to more clearly highlight the link between high values of V and stable (rather than
237 unstable) manifolds, we have computed both stable and unstable manifolds for the Duffing
238 Oscillator flow using a direct method, where we grew manifolds from a small segment starting at
239 the hyperbolic trajectory. For the Duffing Oscillator this computation is straightforward since the
240 the hyperbolic trajectory stays at the origin at all times. Both stable and unstable directly-
241 computed manifolds were then superimposed on a forward-time encounter volume plot in Fig. 4.
242 The comparison shows that, as anticipated, the encounter volume diagnostic clearly highlights
243 stable manifolds as maximizing ridges of V computed in forward time.

244
245 With a variety of dynamical systems techniques available, it is important to understand the
246 advantages and limitation of the different methods. We compared the encounter volume to two
247 well-established and commonly-used methods, the Poincare section (Fig. 3) and the FTLEs (Fig.
248 5). Since the Poincare section requires stroboscopic sampling of trajectories in time, it can only
249 be applied to time-periodic flows, and requires that trajectories are computed over long
250 integration time, typically thousands of the periods of the perturbation. On the other hand, it
251 generally requires only a few parcels to be released at some key locations, rather than releasing a
252 dense grid of initial positions, to map out the entire phase space. The encounter volume and
253 FTLEs, on the other hand, are not limited to time-periodic flows, and also work with
254 significantly shorter segments of trajectories (longest integration time in our simulations in Fig. 2
255 is only 50 periods of perturbation). They are also better suited for identifying manifolds than the
256 Poincare sectioning as they do not require any *a priori* knowledge about the location of the

257 hyperbolic trajectory. On the other hand, they require many more parcels to be released in order
258 to map out the phase space. When applied to the same set of trajectories (same initial positions
259 and integration times), the FTLEs and the encounter volume methods produced similar results
260 (Fig. 5), with V being arguably better suited for 1) identifying the coherent core regions of
261 eddies, where FTLEs have spiraling patterns that complicate the analysis, and 2) producing more
262 continuous segments of manifolds at intermediate integration times, when FTLE-based ridges get
263 discontinuous near the turning points of a manifold. The advantage of FTLEs, on the other hand,
264 is that they have fewer parameters (T and grid spacing), whereas V also depends on R , and that
265 they are less expensive computationally. The more expensive computational cost of V compared to
266 FTLEs is due to two reasons: first, the FTLEs only depend on the initial and final positions of
267 trajectories, whereas V depends on the entire trajectory history; and second, FTLEs depend on
268 the relative distance between a trajectory and its closest neighbors, whereas V keeps tracks of
269 encounters with all trajectories, not just the neighboring trajectories. Thus, the cost of evaluating
270 FTLE for each particle is independent of the total number of particles released, and the cost of
271 evaluating V for each particle increases in proportion to the number of particles (since one needs
272 to keep track of encounters with all particles). The calculation of V is still feasible for realistic
273 geophysical flows, as is illustrated below. Note also that, depending on the physical question
274 being studied, the information about the entire trajectory, not just the final and initial position,
275 might in fact be advantageous.

276
277 Related to issue of computational cost is the question of a sufficient grid size. We have carried
278 out numerical simulations (Fig. 6) to investigate the dependence of the encounter volume on the
279 grid size, and to come up with a rule of thumb recommendation regarding the appropriate grid
280 spacing. Our simulations suggest that the encounter volume values (approximated by $V \approx$
281 $N dV$) are relatively insensitive to the variations of grid spacing between 1/10 and 1/2 of the
282 encounter radius (with the encounter radius being a fraction of the size of the feature of interest,
283 as suggested by Fig. 2), and that the major effect of a coarser grid is the degraded resolution of
284 the resulting V map, rather than incorrect V values.

285

286 b. Bickley Jet

287 The meandering Bickley jet flow is an idealized, but linearly dynamically consistent, model for
288 the eastward zonal jet in the Earth's Stratosphere (del-Castillo-Negrete and Morrison, 1993;
289 Rypina et al., 2007a; Rypina et al., 2011). This flow consists of a steady eastward zonal jet on
290 which two eastward propagating Rossby-like waves are superimposed. All flow parameters used
291 here are identical to those used in our previous 2007 and 2011 papers. In the reference frame
292 moving at a speed of one of the waves, the flow consists of a steady background velocity subject
293 to a time periodic perturbation. The background looks like a meandering jet, with three
294 recirculation gyres to the north and south of the jet core. Between the recirculation gyres, there
295 are three hyperbolic points with the associated stable and unstable manifolds. Under the

296 influence of the time-periodic perturbation imposed by the second wave, heteroclinic tangles are
297 formed by the manifolds emanating from different hyperbolic regions between the recirculations,
298 and a chaotic zone emerges on either side of the jet. The manifolds, however, cannot penetrate
299 through the jet core, which remains regular and acts as a transport barrier separating the northern
300 and southern chaotic zones. All of these features are clearly visible in the Poincare section shown
301 in Fig. 4 (top). The bottom subplot shows the V field computed using the encounter radius
302 $R=5*10^5$, which is about half of the recirculation region radius, and using trajectory integration
303 time on the order of a few winding times within the recirculations. As expected, the encounter
304 volume identified 6 recirculation regions and the jet core as zones with small mixing potential
305 (blue). 6 blue recirculation regions are embedded into two distinct chaotic zones with enhanced
306 mixing potential (yellow-red) on either side of the jet. Mixing potential is the largest (red) along
307 the segments of stable manifolds emanating from the hyperbolic trajectories between
308 recirculations.

309 c. Altimetry-based velocity in the meandering Gulf Stream region

310 Past its separation point from the coast at Cape Hatteras, the strong and narrow Gulf Stream
311 current turns off-shore, where it loses its coherence, broadens and weakens, and starts to
312 meander. Some of the meanders then grow and eventually detach from the current forming
313 strong mesoscale eddies known as the Gulf Stream rings. On 11 July, 1997 a number of such
314 Gulf Stream rings of various strength and size and at different stages of their lifetime were
315 clearly present both north and south of the Gulf Stream Extension Current (Fig. 7).

316 The flow in the Gulf Stream Extension region, with a non-steady meandering jet and the Gulf
317 Stream rings and recirculations to the north and south of the jet core, has a lot in common, at
318 least qualitatively, with the Bickley Jet example. Unlike the idealized model, however, the real
319 Gulf Stream rings have finite lifetimes, and the jet is not periodic in the zonal direction.
320 Nevertheless, many of the qualitative features of the Bickley Jet's V field hold in this example.
321 Specifically, trajectories inside coherent eddy cores have smaller encounter volumes than the
322 eddy peripheries, and the jet centerline has smaller encounter volume than the flanks.

323 The velocity field that we used was downloaded from the AVISO website
324 (<http://www.aviso.altimetry.fr/en/data/products/sea-surface-height-products/global.html>) and
325 corresponds to their gridded product with $\frac{1}{4}$ deg spatial resolution and temporal step of 1 day.
326 This velocity is based on the altimetric sea surface height measurements made from satellites.
327 The heights were converted into velocities using geostrophic approximation. For the encounter
328 volume estimation, trajectories were seeded on a regular grid with $dx = dy \cong 0.06$ deg on 11
329 July 1997 and were integrated forward in time for 90 days using a fifth-order variable-step
330 Runge-Kutta integration scheme with bi-linear interpolation between grid points in space and
331 time. The encounter radius was chosen to be 0.3 deg, which is about a third of the radius of a
332 typical 200-meter-wide Gulf Stream ring.

333 The encounter volume was estimated for three different integration times, $T=30$ days, 60 days
334 and 90 days (Fig. 7). The V field clearly indicates that a number of Gulf Stream rings were
335 present on both sides of the meandering jet. Among those, two strongest ones can be seen at
336 54W, 36N and 52W, 41N, with the low- V (blue) core and high- V (red) periphery. As the
337 integration time increases from 30 days to 90 days, the Gulf Stream rings generally start to leak
338 fluid, their cores start to lose coherence, and the encounter volume within eddy cores starts to
339 increase as more and more trajectories escape into the eddy surroundings over time. After a 90
340 day integration time, only a few Gulf Stream rings still possess coherent cores, whereas others
341 become leaky throughout. Even for the two strongest rings, the coherent Lagrangian cores
342 (bluish regions with $V \approx 0$) shrink down in size and, importantly, become significantly smaller
343 than what the Eulerian velocity field would suggest. The core of the northern eddy also gets
344 shifted slightly to the east from the corresponding Eulerian stagnation point, and becomes
345 deformed into a non-convex sickle-like shape.

346
347 The overall leakiness of the Gulf Stream rings and the small extent of their coherent Lagrangian
348 core regions suggests that the coherent transport by the Gulf stream rings (and maybe by
349 mesoscale eddies in general) over time intervals of a few months or longer may be significantly
350 smaller than what is generally anticipated from Eulerian diagnostics based on closed streamlines
351 or Okubo-Weiss type criteria. Interestingly, the prominent red rings (large V values) around the
352 eddy cores in Fig. 7 indicate that significant contribution to transport by Lagrangian eddies may
353 be due to the high-mixing-potential peripheries rather than the coherent cores themselves.

354
355 To visualize the Lagrangian evolution of the core regions and to illustrate the eddy leakiness, we
356 extracted trajectories from the core of the northern eddy in Fig. 7(left) (i.e., trajectories with
357 $V < 6000 \text{ km}^2$ from the 30-day-long V field), and plotted their subsequent positions after 30
358 days, 60 days and 90 days. The results in Fig. 8 confirm that the eddy core stays completely
359 coherent over 30 days (i.e., all trajectories stay together), but starts to deteriorate at 60 days, with
360 only a small fraction of the initial patch still staying together and the rest of the patch dispersing
361 and forming long and narrow filaments.

362
363 The jet region, although noisy, seems to suggest higher V near the flanks and smaller V near the
364 centerline. The center region is not as well-defined as in the Bickley Jet example, possibly
365 because the Gulf Stream inhibits but does not fully prevent the meridional transport in this
366 region, and because our encounter radius might have been too large to reveal the central region,
367 if the true center region was narrower than $2R$ (0.6 degrees). Finally, the V field suggests that the
368 mixing potential of the flow is not symmetric with respect to the jet centerline and is higher on
369 the northern side. It would be interesting to see if this is a general property of the flow in this
370 region or if this phenomenon is specific to the time interval chosen. This investigation is left for
371 future study.

372

III. Encounter volume for some simple flow regimes

By analogy with molecular diffusion, eddy diffusivity, K , is often used to characterize the eddy-induced downgradient tracer transfer in realistic geophysical fluid flows (LaCasce 2008; Vallis, 2006; Rypina et al., 2015; Kamenkovich et al., 2016). Because of the simplicity of this approach, the majority of existing non-eddy-resolving oceanic numerical models are diffusion based, despite the somewhat questionable assumptions underlying this approach. An analytical connection between the encounter volume and diffusivity would thus be useful for the parameterizations in numerical models.

Although we have not been able to find an analytical expression connecting V and K , we outline below some steps in that direction that help framing the problem. Let us start by considering a simple diffusive random walk particle motion in two-dimensions, where particles take steps of fixed length L in random directions at time intervals Δt . For such process, the single particle dispersion,

$$D = \langle (x - x_0)^2 + (y - y_0)^2 \rangle,$$

which characterizes the mean square displacement from the particle's initial position (x_0, y_0) , grows in proportion to the number of steps, n , i.e.,

$$D = Kn\Delta t,$$

with the proportionality coefficient, $K = L^2 / \Delta t$, denoting the diffusivity. The angular brackets denote ensemble average. We are interested in finding an analytical expression for the encounter number, i.e., the number of particles that pass within radius R from a reference particle over time T , as a function of K and T .

It is convenient to move to a reference frame that is tied to a reference particle, which would then always stay at the origin, while other particles would be involved in a random walk motion. The problem of finding the encounter number then reduces to counting the number of particles that come within radius R from the origin over time T in the moving frame. The properties of the random walk process in the moving reference frame are different from those in the stationary frame. Specifically, the direction of each step in the moving reference frame still remains random (since it is a sum of two random variables, each uniformly distributed within an interval $[0; 2\pi]$), but the step size is no longer fixed. Instead, the step size can be written as

$$L_m^2 = dx_m^2 + dy_m^2 = (dx - dx_{ref})^2 + (dy - dy_{ref})^2 = 2L^2 - 2(dx dx_{ref} + dy dy_{ref}),$$

where dx and dy correspond to displacements of a particle in x and y directions at some instance in time, and subscripts m and ref denote the moving reference frame and the reference trajectory,

405 respectively. Denoting the angle in which the step is taken by φ , the displacements are $dx =$
 406 $L \cos \varphi$, $dy = L \sin \varphi$, $dx_{ref} = L \cos \varphi_{ref}$, $dy_{ref} = L \sin \varphi_{ref}$ leading to

407 $L_m = 2L \sin \alpha$, where $\alpha = \frac{\varphi - \varphi_{ref}}{2}$. Since both φ and φ_{ref} are random variables uniformly
 408 distributed between 0 and 2π , α is a random variable with a flat pdf distribution $\in [0; \pi]$.

409 This change in the step size between the stationary and moving frames leads to a doubling of the
 410 diffusivity in the moving reference frame. To show this, we write down the dispersion in the
 411 moving frame as

$$\begin{aligned}
 D_m &= \langle (x_m - x_{0_m})^2 + (y_m - y_{0_m})^2 \rangle = \\
 &= \langle (x - x_{ref} - x_0 - x_{0ref})^2 + (y - y_{ref} - y_0 - y_{0ref})^2 \rangle = \\
 &= D - 2 \Delta x_{ref} \langle \Delta x \rangle - 2 \Delta y_{ref} \langle \Delta y \rangle + \Delta x_{ref}^2 + \Delta y_{ref}^2 = \\
 &= D + \Delta x_{ref}^2 + \Delta y_{ref}^2,
 \end{aligned}$$

412 where $\Delta x = x - x_0$ is the deviation from the initial position in the stationary frame and similarly
 413 for Δy , Δx_{ref} and Δy_{ref} . We have used $\langle \Delta x \rangle = \langle \Delta y \rangle = 0$ to get the last equality. When
 414 averaged over many reference trajectories, $\langle \Delta x_{ref}^2 + \Delta y_{ref}^2 \rangle = D$ since in the stationary
 415 reference frame the reference particle is doing a random walk just like all other particles, so that
 416 $\langle D_m \rangle = 2D$, or, equivalently, $\langle K_m \rangle = 2K$.

417 We thus seek an expression for the number of particles that are involved in a random walk
 418 process with diffusivity $2K$ and that come within an encounter radius R from the origin during
 419 their first n steps (n plays the role of discretized integration time). This quantity is related to the
 420 first passage time density, which characterizes the probability that a particle has first reached an
 421 absorbing boundary (often referred to as a cliff in statistics) at time t , and its integral quantity,
 422 called the survival probability, which characterizes the probability that a particle has not come in
 423 contact with absorbing boundary over time t (i.e., it survived after time t without falling off a
 424 cliff). So far, however, we have not been able to complete the derivation and we leave this
 425 development for a future investigation.

426 Numerical Monte-Carlo simulations of a random walk process suggest that the dependence of
 427 the encounter number (and encounter volume) on the integration time T is not a linear and not a
 428 square-root function. The power-law least square fit of the form $V \sim T^\alpha$ returns α values between
 429 0.64 and 0.78 for a wide variety of R and K , each spanning an order of magnitude interval of
 430 values. Similarly, the power-law least square fit $V \sim K^\beta$ and $V \sim R^\gamma$ yield $\beta \cong 0.664$ and $\gamma \cong$
 431 0.69.

432 The ballistic spreading that is dominated by a local velocity shear is another commonly-
 433 encountered spreading regime. There, the separation between particles grows in proportion to
 434 time. Ballistic spreading can often be observed in nonsteady realistic oceanic flows at time scales
 435 that are much shorter than the onset of diffusive spreading (which develops after a trajectory
 436 samples multiple different eddies or other flow features). To derive a connection between
 437 encounter volume and velocity shear, consider a trajectory that is advected by a flow field with
 438 constant meridional velocity shear, γ , of zonal velocity. In a reference frame moving with a
 439 reference trajectory the velocity profile is, $u(y) = \gamma y$ where u denotes the x-component of
 440 velocity, and the encounter volume becomes

$$441 \quad V \cong N dx dy = 2 \int_0^R dy \int_R^{R+x(T)} dx = 2 \int_0^R dy \int_0^T u(y) dt = \gamma R^2 T, \quad (2)$$

442 suggesting a linear growth with time for a ballistic regime. Note that expression (2) quantifies the
 443 encounter volume as a volume of fluid that is initially located outside of the encounter sphere
 444 and that passes through the sphere over time T . To include the volume of fluid that is initially
 445 located within the encounter sphere (or within the encounter circle in this 2D case), one needs to
 446 add πR^2 to expression (2). The contribution of this term gets negligibly small as $T \rightarrow \infty$.
 447 Expression (2) has been tested numerically and shows good agreement with the numerically-
 448 estimated encounter volume for a linear shear flow (Fig. 10(right)).

449 The steady linear saddle flow with a constant strain rate α and velocities

$$450 \quad u = \alpha x; v = -\alpha y. \quad (3)$$

451 is another commonly-considered example often used to approximate the vicinity of a hyperbolic
 452 trajectory in more complicated non-steady non-linear situations. A unique property of this flow is
 453 that the velocity profile is unchanged in any reference frame moving with a trajectory. This can
 454 be shown by applying the coordinate transformation, $\hat{x} = x - x_{tr}(t)$; $\hat{y} = y - y_{tr}(t)$, where
 455 $(x; y)$ are coordinates in a stationary frame, $(\hat{x}; \hat{y})$ are coordinates in a moving frame, and
 456 $(x_{tr}(t); y_{tr}(t))$ is the trajectory. The velocity in a moving frame is then

$$457 \quad \begin{aligned} \hat{u} &= u - \frac{dx_{tr}}{dt} = \alpha x - \frac{dx_{tr}}{dt} = \alpha \hat{x} + \alpha x_{tr} - \frac{dx_{tr}}{dt} = \alpha \hat{x} \\ \hat{v} &= v - \frac{dy_{tr}}{dt} = -\alpha y - \frac{dy_{tr}}{dt} = -\alpha \hat{y} - \alpha y_{tr} - \frac{dy_{tr}}{dt} = -\alpha \hat{y} \end{aligned} \quad (4)$$

458 where the last equality holds because $\frac{dx_{tr}}{dt} = \alpha x_{tr}$; $\frac{dy_{tr}}{dt} = -\alpha y_{tr}$. Thus, without loss of
 459 generality, we can consider a flow in a reference frame moving with a reference trajectory that is
 460 located at the origin. The encounter volume that comes within a radius R of the origin over the
 461 time interval T can be written as

462 $V \cong N dx dy = \int_0^T F_{\perp}(t) dt,$
 463 (5)

464 where dx and dy denote the grid spacing between neighboring trajectories, and the flux of
 465 trajectories entering the circle is given by

466 $F_{\perp} = \int u_{\perp} ds.$ (6)

467 Again, as in our treatment of the linear shear flow, expression (5) does not include the volume of
 468 fluid that is initially located within the encounter sphere (or encounter circle in this 2D case), but
 469 only the volume that was initially located outside but passes through the sphere over time T . The
 470 contribution of that fixed volume (πR^2), gets negligibly small as $T \rightarrow \infty$. Here u_{\perp} is the inward-
 471 looking normal component of velocity at a circle of radius R , and ds is an infinitesimal segment
 472 of the circle arc. From symmetry, the flux is the same in each of the 4 quadrants so we will
 473 consider the 1st quadrant only. From geometry (Fig. 11),

474 $u_{\perp} = -u \sin \beta - v \cos \beta = \alpha R (\cos^2 \beta - \sin^2 \beta)$ and $ds = R d\beta$, leading to

475 $F_{\perp}^{1st\ quad} = \alpha R^2 \int_0^{\pi/4} (\cos^2 \beta - \sin^2 \beta) d\beta = \frac{\alpha R^2}{2}$ (7)

476 and

477 $V^{1st\ quad} = \int_0^T F_{\perp}(t) dt = \alpha R^2 T / 2.$ (8)

478 Adding the other 3 quadrants then gives

479 $V = 2\alpha R^2 T.$ (9)

480 Numerical simulations of the encounter volume in a linear strain flow show excellent agreement
 481 with theoretical expression (9) (Fig. 10(left)).

482 The linear growth of the encounter volume with time in the linear shear and linear strain flows
 483 could be anticipated by noting that both flows are steady in a reference frame moving with a
 484 reference trajectory, and all particles only encounter the origin once and never come back. Thus,
 485 the flux through the encounter circle is constant in time and the encounter volume, which is a
 486 time-integral of flux, is proportional to time. The random walk flow seems to be different
 487 because the particles can encounter the reference trajectory more than once, leading to a non-
 488 steady flux of first encounters and a non-linear time dependence of the encounter volume.

489 IV. Mixing potential for a specified tracer: the \mathbf{u}^* -approach

490 The above examples are centered on mixing potential of a flow field, but there may be value in
 491 computing the encounter volume for swarms of trajectories of biological organisms, drifting
 492 sensors, and other non-Lagrangian trajectories. For example, if one is interested in the actual
 493 transport of scalar properties such as heat, salt, or vorticity, then it may be useful to calculate V
 494 using a velocity field that is directly linked to the vector flux of the scalar of interest. This
 495 approach has been used in connection with heat transport in advective/diffusive flow (Bejan,
 496 1995; Costa, 2006; Mahmud and Fraser 2007; Mukhopadhyay et al., 2002, and Speetjens, 2012)
 497 and more recently with the transport of more general scalars in forced and dissipative (and
 498 possibly turbulent) flows (Pratt et al., 2016). The central idea is to define velocity field \mathbf{u}^*
 499 based on the (known) flux \mathbf{F} of a scalar with concentration C . Here bold quantities denote
 500 vectors. The concentration is assumed to obey a conservation equation of the form

$$501 \quad \frac{\partial C}{\partial t} = -\nabla \cdot \mathbf{F} + S, \quad (10)$$

502 where S contains the sources and sinks of C . The velocity \mathbf{u}^* is defined as the velocity of a
 503 hypothetical flow in which the flux of C is purely advective: $\mathbf{F} = C\mathbf{u}^*$. Pratt et al., 2016 show
 504 that, in the absence of sources or sinks of C , that the total amount of C contained within any
 505 material boundary advected by this hypothetical flow is conserved: $\frac{d}{dt} \int_V C dV = 0$. Thus \mathbf{u}^* is
 506 linked to scalar property fluxes while \mathbf{u} is limited to fluid volume (or area) fluxes.

507 If indeed \mathbf{F} is due entirely to advection by the actual fluid velocity field \mathbf{u} , then $\mathbf{u}^* = \mathbf{u}$, but more
 508 generally \mathbf{F} will contain contributions from eddy fluxes, molecular or sub-grid diffusion, and
 509 even forcing and dissipation terms that can be expressed as the divergence of a flux. In addition,
 510 \mathbf{F} may be augmented by the addition of any non-divergent vector without altering Eq. (3). As
 511 shown by Speetjens (2012), this lack of uniqueness can be dealt with by defining a physically
 512 relevant reference scalar distribution and then focusing on the flux of the scalar anomaly, an
 513 approach we adapt below. Thus, by estimating the encounter volume V for trajectories of the \mathbf{u}^*
 514 field, one is quantifying the rate at which different ‘parcels’ of tracer anomaly are brought into
 515 contact with each other. An example is presented next.

516 a. Example: encounter volume for a tracer with a specified initial distribution in a
 517 Bickley Jet flow

518 In this subsection we apply the encounter volume diagnostic to quantify the mixing potential for
 519 a specific tracer in the Bickley Jet flow. Our goal is to describe an example where the \mathbf{u}^* field for
 520 a given tracer is significantly different from the flow velocity \mathbf{u} , and where the corresponding
 521 encounter volume field for a given tracer, V^* , is significantly different from the water particle
 522 trajectory-based encounter volume V .

523 Consider the Bickley Jet flow with the same parameters as in II(b) and assume that one is
 524 interested in a tracer that, at initial time t_0 , has uniform value c_0 south of the jet and has a

525 constant meridional gradient north of the jet, i.e., $C_0 = c_0 + 0.5y(\text{sign}(y - 5 * 10^5) + 1)$ with
 526 $c_0 = 1$. Ignoring the diffusive terms, the tracer evolution is governed by the advection
 527 equation $\frac{\partial c}{\partial t} = -\nabla(\mathbf{u} \cdot C)$, where \mathbf{u} is the Bickley Jet flow velocity. Since the jet core acts as a
 528 transport barrier separating the northern and southern chaotic zones, this tracer will rapidly
 529 filament and develop high property gradients north of the jet, but will remain uniform south of
 530 the jet. So, despite the fact that the mixing potential of the Bickley Jet flow is exactly the same
 531 on both sides of the jet (Fig. 7(bottom)), stirring will not lead to mixing for this particular tracer
 532 distribution south of the jet, where tracer gradient is zero, thus leading to zero mixing potential
 533 for this particular tracer. We seek to capture this effect via applying the encounter volume-based
 534 mixing diagnostic to the corresponding \mathbf{u}^* field for this tracer.

535 In the spirit of Speetjens (2016) we regard c_0 as the reference concentration, here constant, and
 536 define \mathbf{F} to be the flux of a tracer anomaly: $\mathbf{F} = \mathbf{u} \cdot (C - c_0)$. The resulting $\mathbf{u}^* = \frac{\mathbf{F}}{c} = \mathbf{u} \left(1 - \frac{c_0}{c}\right)$
 537 is zero south of the jet where $C = c_0$ and is approximately equal to \mathbf{u} north of the jet where
 538 $C \gg c_0$, leading to the \mathbf{u}^* -based encounter number $V^* = 0$ south of the jet and $V^* \approx V$ north of
 539 the jet.

540 This behavior was further validated numerically in Fig. 12, where we first numerically simulated
 541 the evolution of this tracer in the Bickley Jet flow, then estimated \mathbf{u}^* , counted N^* and estimated
 542 $V \cong NdV$ for trajectories advected by the \mathbf{u}^* field. The result confirms that mixing potential for
 543 this tracer is zero south of the jet, $V^* = 0$, whereas north of the jet V^* is very close to V from
 544 Fig. 7(bottom). Thus, by combining the \mathbf{u}^* approach with the encounter volume idea, we were
 545 able to correctly capture the mixing potential for a specific tracer.

546 V. Summary and discussion

547 When water parcels come in direct contact with each other, they can exchange water properties,
 548 leading to mixing. The trajectory encounter volume, V , quantifies the volume of fluid that passes
 549 close to a reference trajectory over a time interval $t_0 < t < t_0 + T$. Thus, the encounter volume
 550 is proportional to, and can be used as a measure of, the mixing potential of a flow. For
 551 incompressible flows densely seeded with particles, the encounter volume can be approximated
 552 by $V \cong N\delta V$ where N is the encounter number, i.e., the number of trajectories that come
 553 within radius R from the reference trajectory over time $t_0 < t < t_0 + T$, and δV is a small
 554 volume element.

555 The encounter volume diagnostic was tested in 3 flows with increasing complexity, the Duffing
 556 Oscillator, the Bickley Jet, and the altimetry-based velocity in the Gulf Stream Extension region.
 557 In all cases, V was smaller within cores of coherent eddies and jets, where mixing potential was
 558 low, and V was larger in chaotic zones near the peripheries of the eddies and at the flanks of the
 559 meandering jets, where the mixing potential of the flow was high.

560 Similar to finite-time Lyapunov exponents (FTLEs) that are commonly used to delineate regions
561 with qualitatively different motion (Haller, 2002; Shadden et al., 2005; Lekien and Ross, 2010),
562 V depends on the trajectory starting time, t_0 , allowing tracking the evolution of oceanic features
563 by repeating the calculation at different t_0 , and on the trajectory integration time, T , revealing
564 different structures that impact the mixing potential of the flow from time t_0 to time $t_0 + T$.
565 Specifically, longer segments of stable/unstable manifolds emanating from hyperbolic regions
566 are revealed for longer T in forward/backward time. In the long- T limit, when both the stable and
567 unstable manifolds densely fill the entire chaotic zone, V approaches a constant equaling to the
568 volume of the chaotic zone.

569 V also depends on the encounter radius R , which defines how close two trajectories need to be in
570 order to be counted as an encounter. Analytic arguments and numerical simulations both suggest
571 that R on the order of a fraction ($\sim 1/3$) of the radius of the smallest feature of interest should
572 work well in most cases.

573 Finally, while V was initially introduced in the continuous limit of infinitely many infinitely
574 small fluid elements (i.e., infinitely dense grid of initial positions), its approximation $V \cong N\delta V$
575 depends on the initial spacing between neighboring trajectories. Numerical simulations suggest
576 that this approximation works well for grid spacing as large as $R/2$ (with the appropriately
577 chosen R as discussed above), and that the major effect of increasing the grid spacing is in the
578 degraded resolution of the resulting V -map rather than incorrect V values.

579 As with FTLEs, complexity measures (Rypina et al., 2011), Lagrangian descriptors (Mendoza et al.,
580 2014) and other techniques from the dynamical systems theory (Beron-Vera et al., 2013;
581 Budisic and Mezic, 2012; Froyland et al., 2007; Haller et al., 2016), V can be computed for
582 forward and backward in time trajectories, with the backward computation revealing unstable
583 manifolds. Our encounter number could plausibly be related, in a limiting case, to the mixing
584 geometry of Karrash and Keller, 2017.

585 For a ballistic spreading regime dominated by the velocity shear γ , and for the linear saddle flow
586 with a constant strain α , V was shown to be proportional to γt and αt , respectively. The linear
587 growth of the encounter number with time for the linear shear and linear strain flows is a
588 consequence of the steady flux of first encounters through the encounter circle.

589 An analytical connection between the encounter volume and a widely-used measure of mixing,
590 the diffusivity K , would be a desirable result for parameterizing the effects of eddies in
591 numerical models. Some initial developments towards deriving such a formula were outlined for
592 a diffusive random walk process. It was shown numerically that the dependence of V on time is
593 non-linear, but numerical simulations were too inconclusive to make further inferences.

594 The mixing potential is the property of the flow field and characterizes the intensity of stirring,
595 whereas the actual tracer mixing depends both on the flow and the tracer. For example, no tracer

596 mixing will occur if the tracer gradient is zero, even if the mixing potential of the flow is high.
597 To address this, we have proposed combining the encounter number diagnostic with the \mathbf{u}^* -
598 approach of Pratt et al, 2016 for characterizing the mixing potential for a specific tracer C . \mathbf{u}^*
599 depends on, and includes information about, the tracer fluxes. In the absence of sources and sinks
600 of C , the amount of tracer is conserved within any Lagrangian volume advected by \mathbf{u}^* , so the
601 encounter volume V^* computed for trajectories advected by \mathbf{u}^* can be used to quantify the
602 mixing potential for a specific tracer. An example was presented where V^* for a specified tracer
603 distribution in the Bickley Jet flow was significantly different from V in a large part of the
604 domain.

605 The encounter volume is a frame-independent quantity because it is based on relative distances
606 between water parcel trajectories, rather than on properties of isolated trajectories. The encounter
607 volume values do not change under orthogonal transformations of coordinates, i.e., under
608 rotations and translations of a reference frame. This is a desirable property because the ability of
609 a flow to mix tracers should not depend on the reference frame.

610 The encounter volume and, more generally, encounter mass ideas presented in this paper are not
611 restricted to two dimensions and can be used to quantify mixing potential in three-dimensional
612 flows. This framework also does not require incompressibility and can work with unstructured
613 irregular grids. The investigation of the performance of the method in quantifying mixing
614 potential of a flow in such more complicated cases is left for a future study.

615 **Acknowledgments:** This work was supported by the NSF grants OCE-1154641, OCE-1558806
616 and EAR-1520825, ONR grant N00014-11-10087 and NASA grant NNX14AH29G.

617

618

619

620

621

622

623

624

625

626

627

628 **References:**

629 Allshouse, M. R. and J.-L.T., Detecting coherent structures using braids, *Physica D* **241** (2), 95–
630 105, January 2012.

631 **Bejan, A.,1995. *Convection Heat Transfer*, Wiley, New York (1995).**

632 Beron-Vera, F. J., Wang, Y., Olascoaga, M. J., Goni, J. G., and G. Haller, “Objective detection
633 of oceanic eddies and the Agulhas leakage,” *J. Phys. Oceanogr.* **43**, 1426–1438 (2013).

634
635 Budisic, M. and Mezic, I., “Geometry of the ergodic quotient reveals coherent structures in
636 flows,” *Physica D* **241**, 1255–1269 (2012).

637
638 **Costa, V.A.F. 2006. Bejan’s heatlines and masslines for convection visualization and analysis,**
639 ***Appl. Mech. Rev.* **59**, 127.**

640 del-Castillo-Negrete, D., and P. J. Morrison, 1993: Chaotic transport by Rossby waves in shear
641 flow. *Phys. Fluids A*, **5**, 948–965.

642
643 Froyland, G., Padberg, K., England, M. H., and Treguier, A. M., “Detection of coherent oceanic
644 structures via transfer operators,” *Phys. Rev. Lett.* **98**, 224503 (2007).

645
646 Froyland, G. and K. Padberg-Gehle. Finite-time entropy: a probabilistic approach for measuring
647 nonlinear stretching. *Physica D*, **241**(19):1612-1628, 2012

648
649 Haller, G.: Lagrangian coherent structures from approximate velocity data, *Phys. Fluid*, **14**,
650 1851–1861, 2002.

651
652 Haller, G., A. Hadjighasem, M. Farazmand and F. Huhn, 2016: “Defining coherent vortices
653 objectively from the vorticity,” *J. Fluid Mech.* (2016), vol. 795, pp. 136_173.
654 doi:10.1017/jfm.2016.151

655
656 Kamenkovich, I., I. Rypina, and P. Berloff, 2015: Properties and Origins of the Anisotropic
657 Eddy-Induced Transport in the North Atlantic. *J. Phys. Oceanogr.*, **45**, 778–791, doi:
658 10.1175/JPO-D-14-0164.1.

659
660 Karrash, D., and J. Keller, 2017: A geometric heat-flow theory of Lagrangian coherent
661 structures. NPG, *submitted*

662
663 LaCasce, J. H., 2008: Lagrangian statistics from oceanic and atmospheric observations.
664 Transport and Mixing in Geophysical Flows, J. B. Weiss and A. Provezale, Eds., Springer, 165–
665 228. Cambridge University Press, 745 pp.

666

667 Lekien, F. and Ross, S. D.: The computation of finite-time Lyapunov exponents on unstructured
668 meshes and for non- Euclidean manifolds, *Chaos*, 20, 017505, doi:10.1063/1.3278516, 2010
669

670 Mahmud, S. , R. A. Fraser, 2007. Visualizing energy flows through energy streamlines and
671 pathlines, *Int. J. Heat Mass Transfer* **50**, 3990.

672 Mendoza, C., Mancho, A. M., and Wiggins, S., “Lagrangian descriptors and the assessment of
673 the predictive capacity of oceanic data sets,” *Nonlinear Process. Geophys.* 21, 677–689 (2014).
674

675 Mukhopadhyay, A., X. Qin, S. K. Aggarwal, I. K. Puri, 2002. On extension of “heatline” and
676 “massline” concepts to reacting flows through use of conserved scalars, *ASME J. Heat Transfer*
677 **124**, 791.

678 Pratt, L., R. Barkan, and I. Rypina, 2016: “Scalar flux kinematics,” *Fluids* 2016, 1, 27;
679 doi:10.3390/fluids1030027
680

681 Rypina, I. I., Scott, S. E., Pratt, L. J., and Brown, M. G., “Investigating the connection between
682 complexity of isolated trajectories and lagrangian coherent structures,” *Nonlinear Proc. Geophys.*
683 18, 977–987 (2011).
684

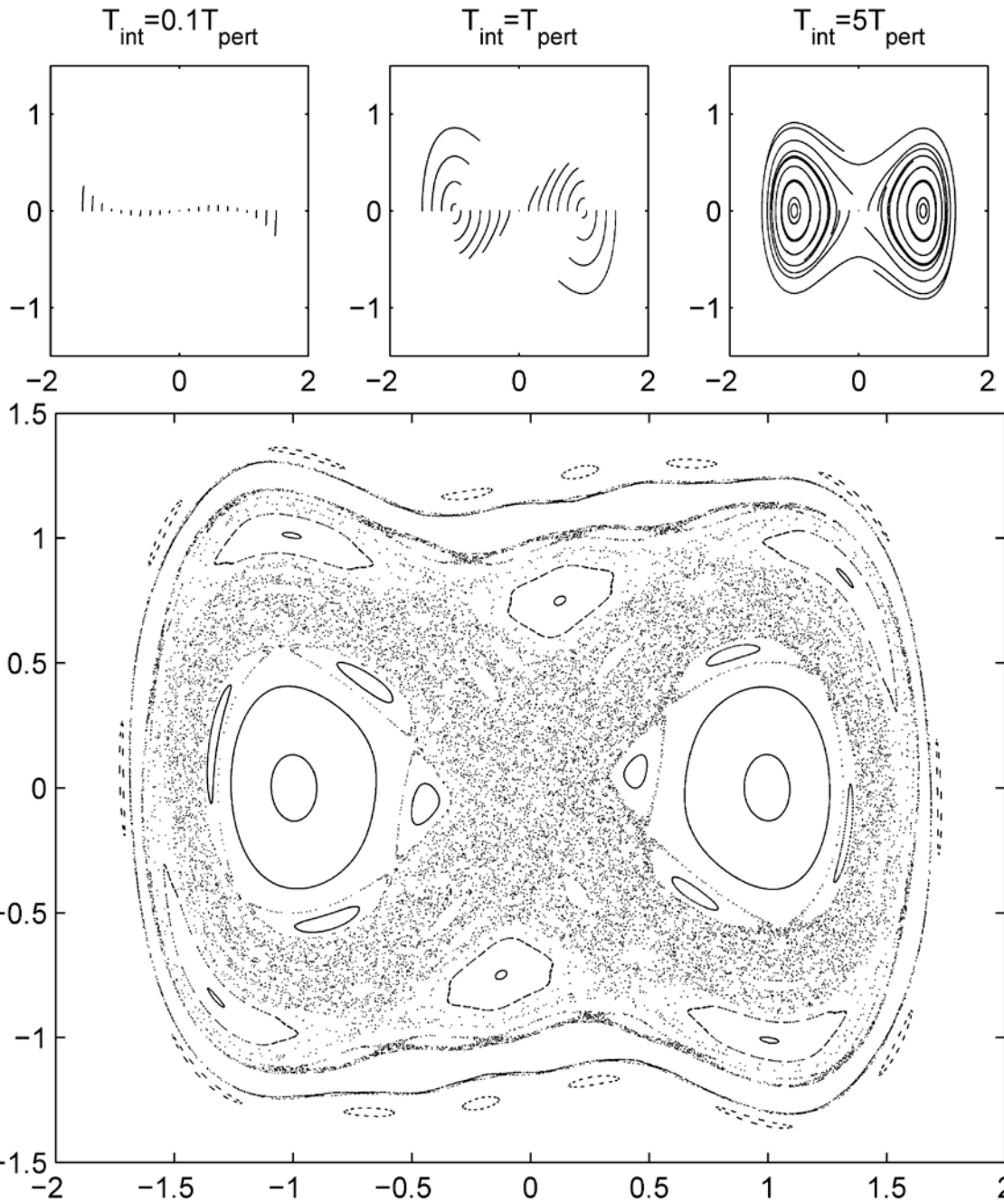
685 Rypina, I. I., Brown, M. G., Beron-Vera, F. J., Kocak, H., Olascoaga, M. J., and
686 Udovydchenkov, I. A.: On the Lagrangian dynamics of atmospheric zonal jets and the
687 permeability of the Stratospheric Polar Vortex, *J. Atmos. Sci.*, 64, 3593–3610,
688 2007a.

689 Rypina, I., I. Kamenkovich, P. Berloff, and L. Pratt, 2012: Eddy-induced particle dispersion in
690 the near-surface North Atlantic. *J. Phys.*
691 *Oceanogr.*, 42, 2206–2228, doi:10.1175/JPO-D-11-0191.1.

692 Speetjens, M. F. M., 2012. A generalised Lagrangian formalism for thermal analysis of laminar
693 convective heat transfer, *Int. J. Therm. Sci.* **61**, 79.

694 Shadden, S. C., Lekien, F., and Marsden, J. E.: Definition and properties of Lagrangian coherent
695 structures from finite-time Lyapunov exponents in two-dimensional aperiodic flows, *Physica D*,
696 212, 271–304, 2005.
697

698 Vallis, G. K., 2006: *Atmospheric and Oceanic Fluid Dynamics*.
699
700
701
702
703



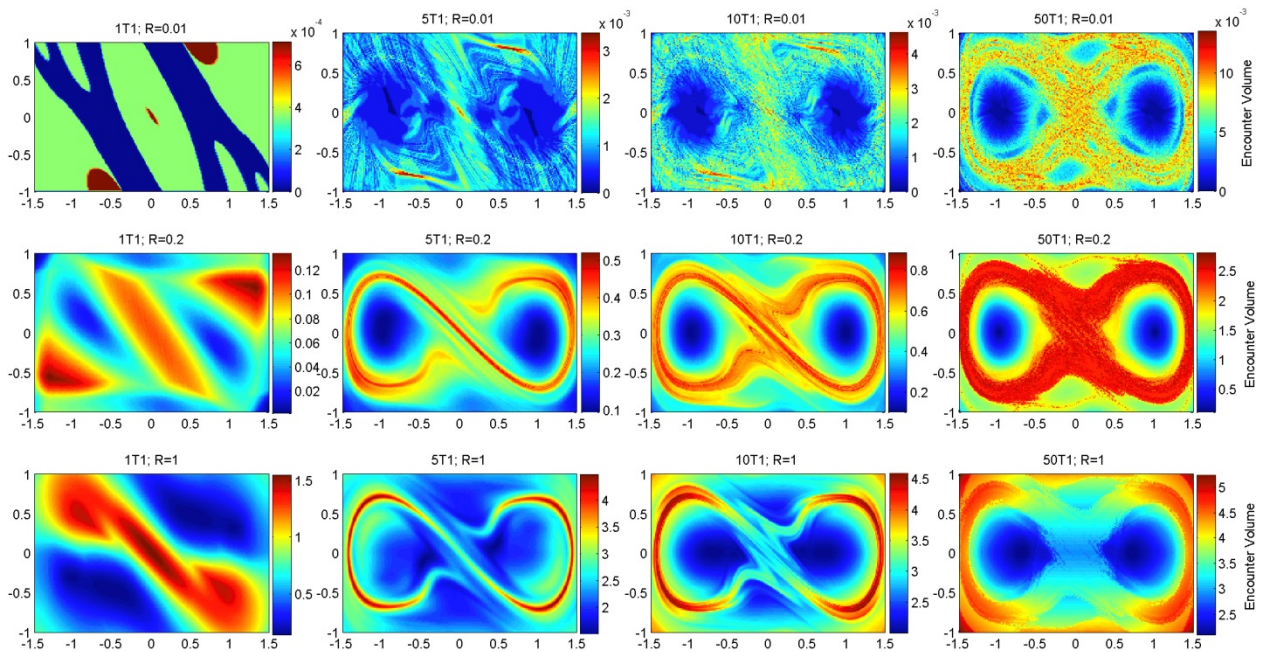
704

705

706

707

Figure 1. Trajectory segments for different integration times (top) and Poincaré section (bottom) for the Duffing Oscillator



709

710

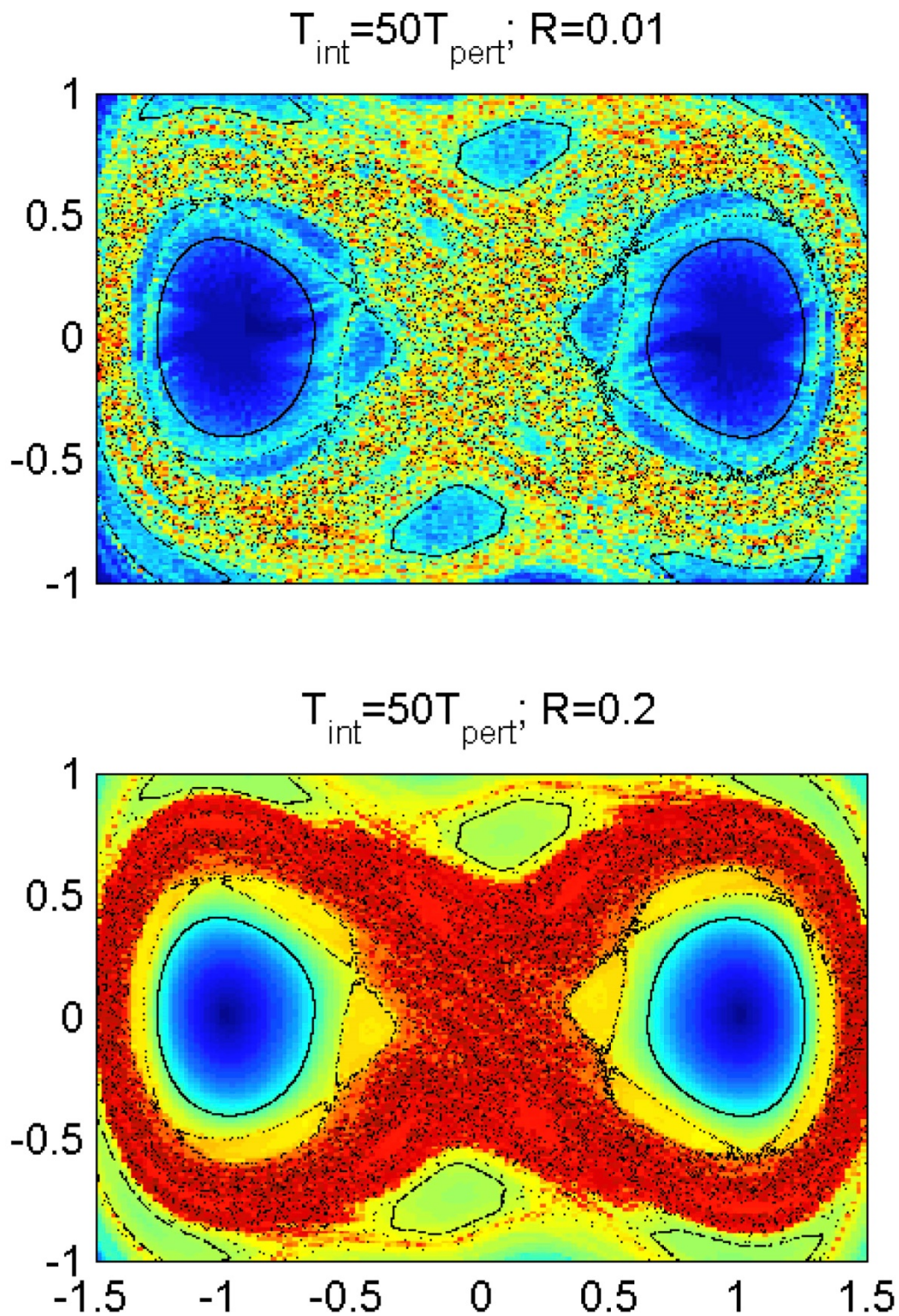
711

712

713

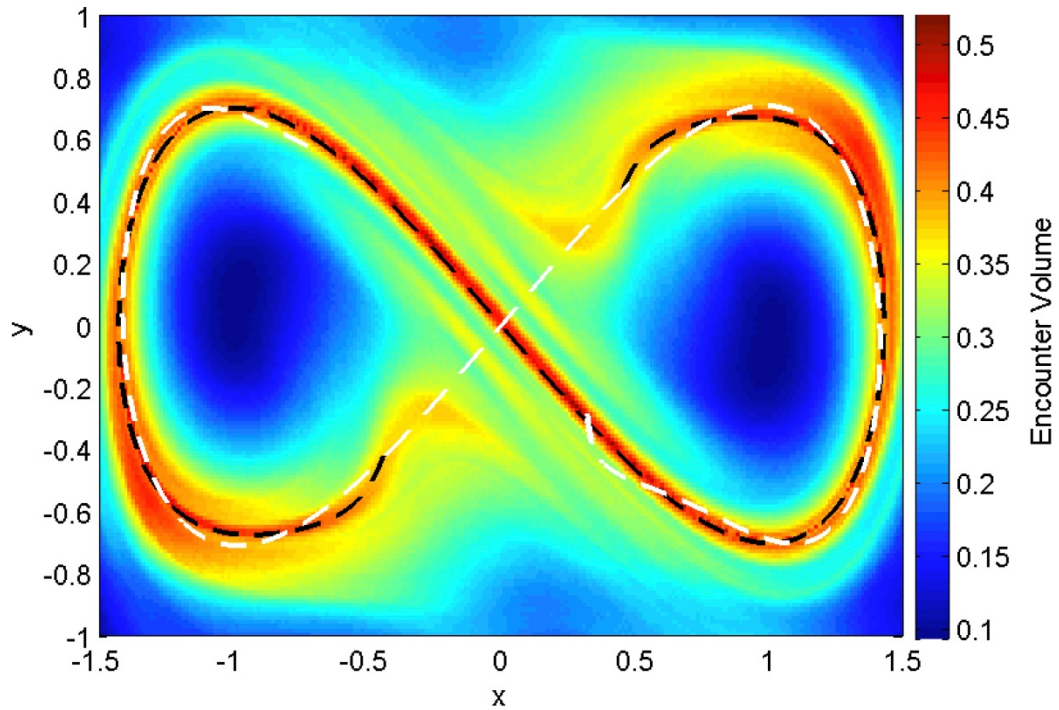
714

Figure 2. Encounter volume for the Duffing Oscillator for various integration times, from $T=0.1T_{\text{pert}}$ (on the left) to $T=50T_{\text{pert}}$ (on the right), and for various encounter radii, from $R=0.01$ (on the top) to $R=1$ (on the bottom). Trajectories were released on a regular grid spanning the entire domain with grid spacing of 0.013 in both x and y directions.



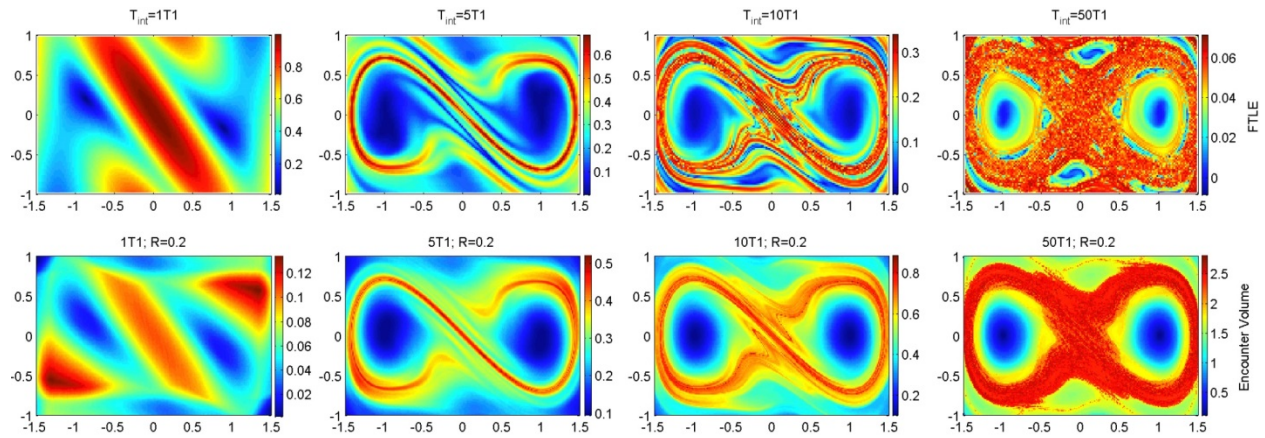
715

716 **Figure 3. Poincaré section (black dots; same as in the bottom panel of Fig. 1) superimposed**
 717 **onto the encounter volume (color; same as top and middle right panels in Fig. 2). Only**
 718 **select trajectories from the Poincaré section are shown.**



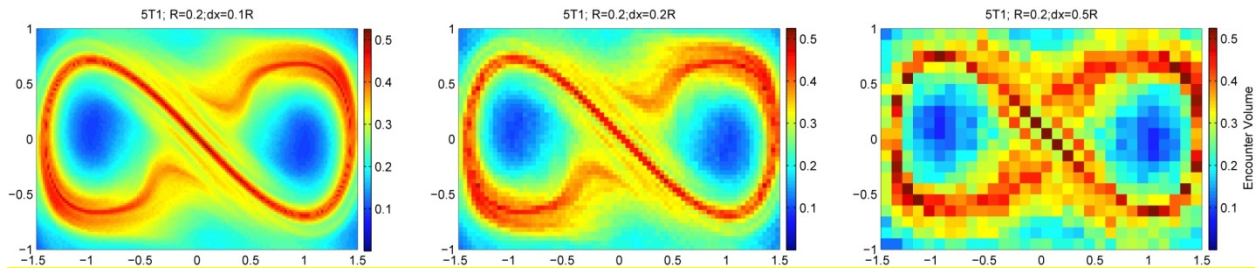
719
 720
 721
 722
 723
 724
 725
 726
 727
 728
 729
 730
 731
 732
 733
 734

Figure 4. Encounter Volume (color; the same as 2nd row and 2nd column subplot of Fig. 2) and stable (black) and unstable (white) manifolds for the Duffing Oscillator flow computed using the direct method.



735
 736 **Figure 5. Comparison between the FTLEs (top) and the encounter volume (bottom; same**
 737 **as middle row of Fig. 2) for the Duffing Oscillator flow for various integration times, from**
 738 **$T=0.1T_{\text{pert}}=0.13$ (on the left) to $T=50T_{\text{pert}}=66.67$ (on the right). The same set of**
 739 **trajectories, deployed on a dense initial grid with 0.02 grid spacing is used in all**
 740 **simulations. In the bottom panels, $R=0.2$.**

741
 742
 743
 744
 745
 746
 747
 748
 749
 750
 751
 752
 753
 754
 755



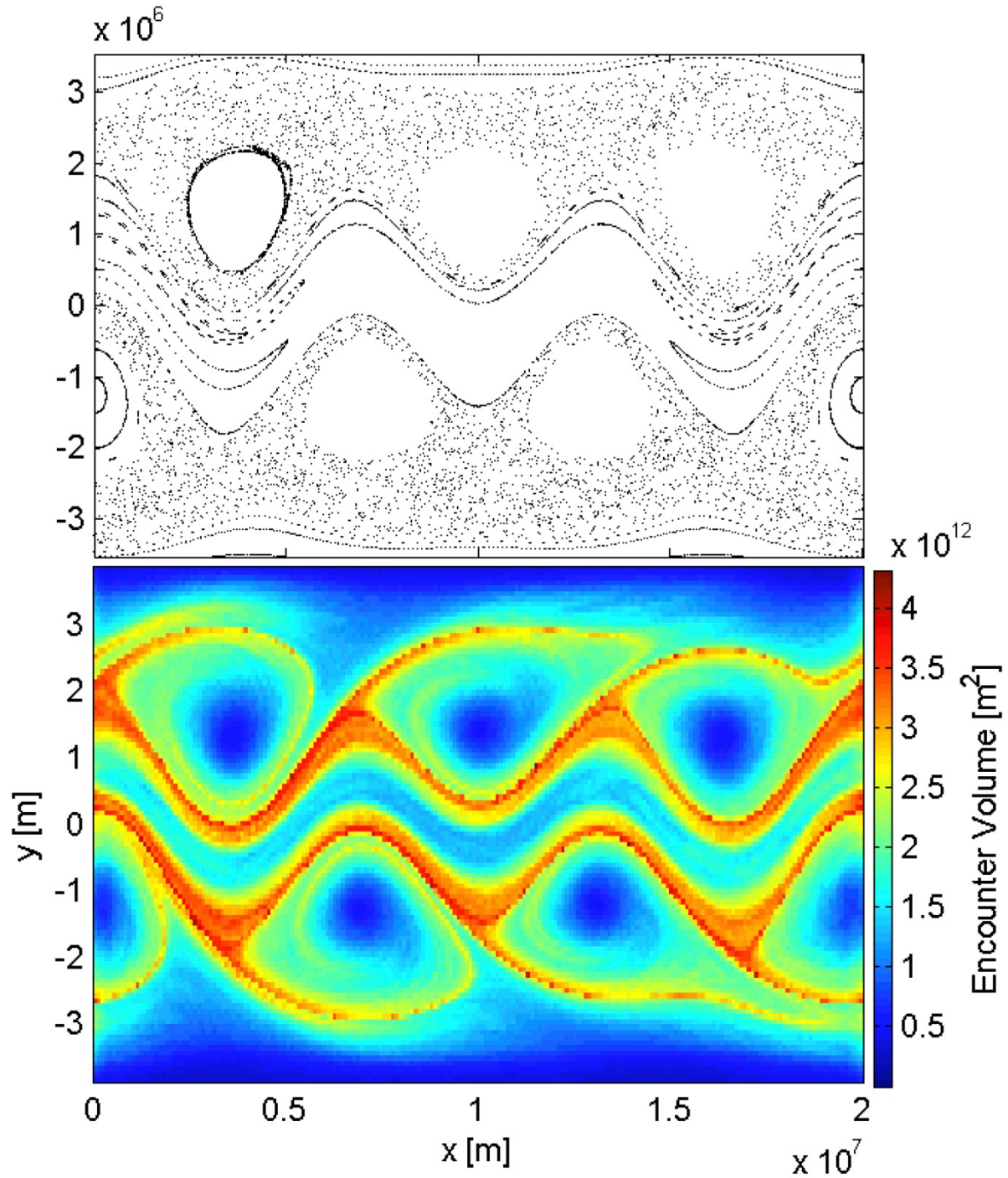
756

757 **Figure 6. Encounter volume, V , for the Duffing Oscillator flow for various grids of initial**
 758 **positions, from dense grid spacing of 0.02 (left), to intermediate grid spacing of 0.04**
 759 **(middle), to coarse grid spacing of 0.1 (right). Encounter radius, $R=0.2$, and integration**
 760 **time, $T=6.67$, are the same in all 3 simulations.**

761

762

763



764

765 **Figure 7. Poincaré section (top) and encounter volume V (bottom) for the Bickley Jet flow.**

766 **For the V calculation, trajectories were released on a regular grid spanning the entire**

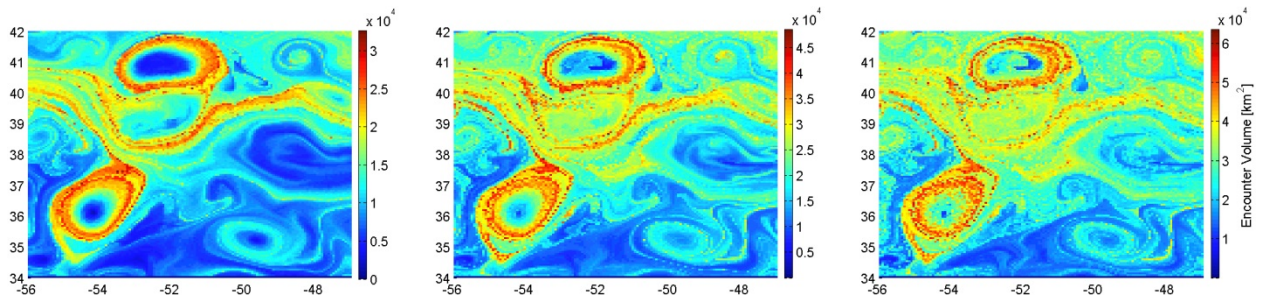
767 **domain with grid spacing of about 10^5 in both x and y directions.**

768

769

770

771



772 **Figure 8. Encounter volume for the AVISO velocities in the Gulf Stream Extension region**
773 **for trajectories released on 7/11/1997 and integrated over 30 days (left), 60 days (middle)**
774 **and 90 days (right). Trajectories were released on a regular grid spanning the domain from**
775 **65W to 35W and from 30N to 50N with grid spacing of about 0.06 deg in both longitude**
776 **and latitude. Additional simulations were performed to insure that the release domain was**
777 **sufficiently large, and that further increase of the release domain does not lead to changes**
778 **in the encounter volume for trajectories starting in the subdomain shown.**

779

780

781

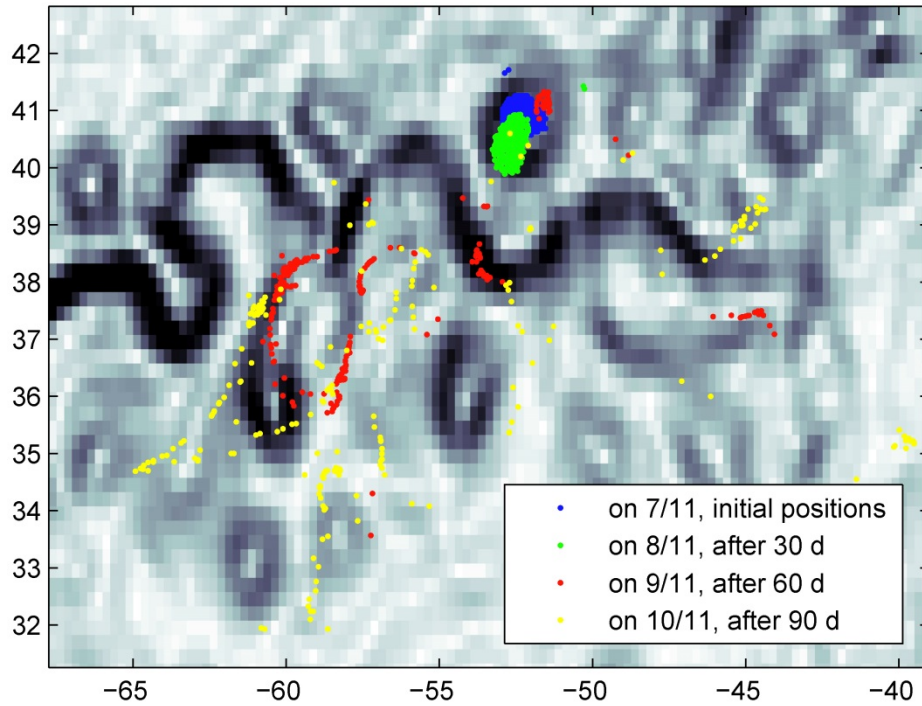
782

783

784

785

786



787

788 **Figure 9. Positions of trajectories that were initially located within the eddy core on**
 789 **7/11/1997 (blue patch) after 30 days (green), 60 days (red) and 90 days (yellow) of**
 790 **integration. Background shows the flow kinetic energy snapshot on 7/11/1997.**

791

792

793

794

795

796

797

798

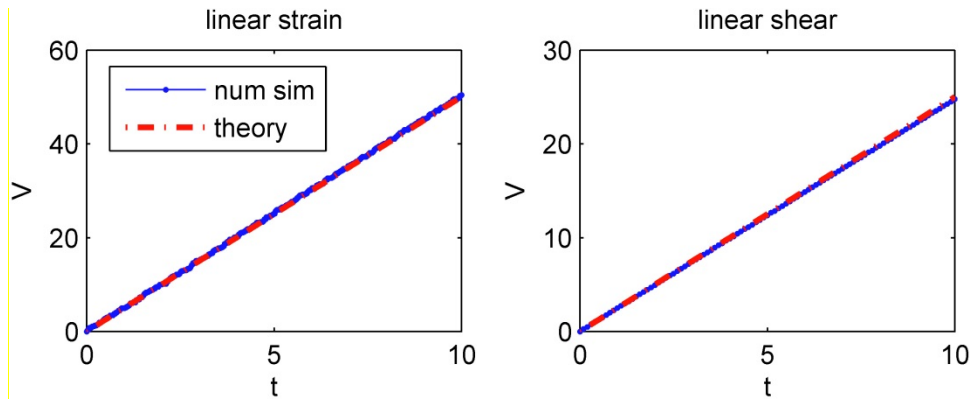
799

800

801

802

803



804

805

806

807

808

809

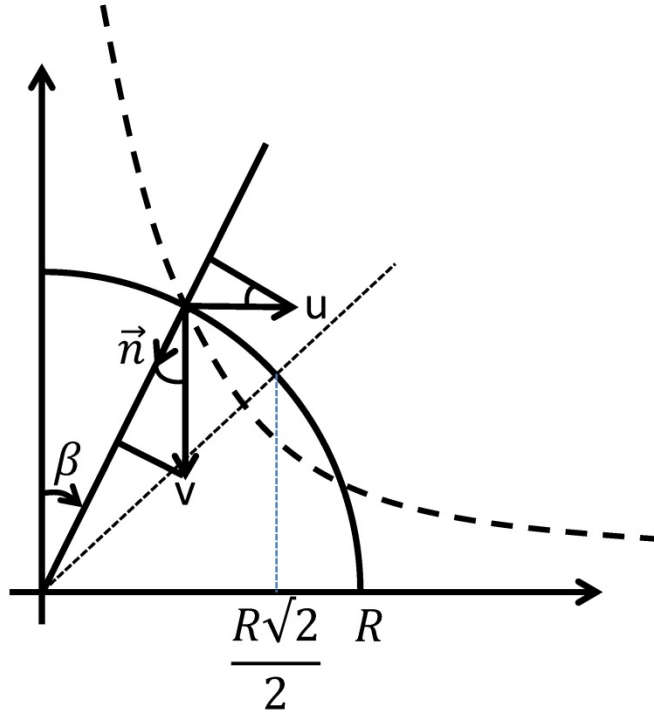
Figure 10. Comparison between numerically computed encounter volume (blue) and analytical predictions (eqs. (8) and (9)) (red) for the linear strain (left) and linear shear flows (right). For the linear shear flow $\alpha=0.1$, $R=5$, $dx=dy=R/25$; for the linear strain flow $\gamma=0.1$, $R=5$; $dx=dy=R/25$. Other parameter choices show good agreement as well.

810

811

812

813



814

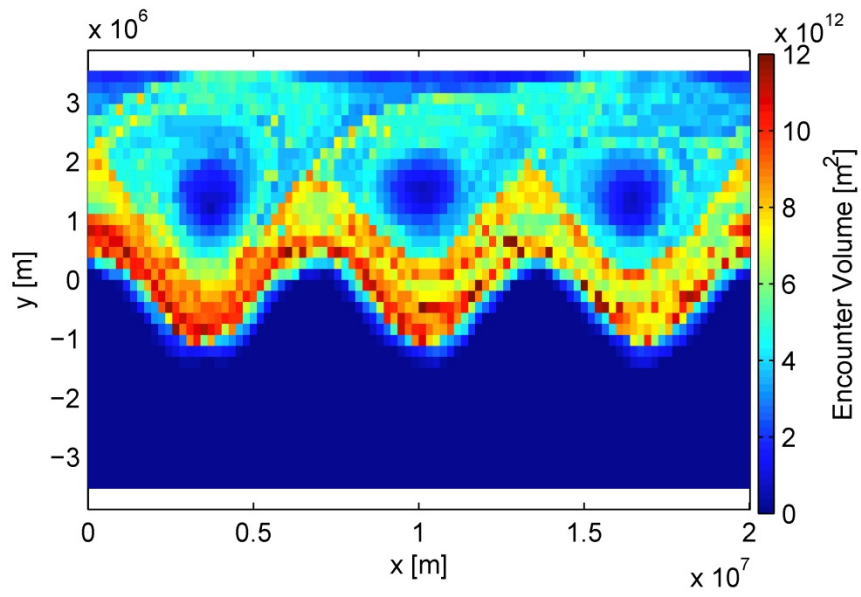
815 **Figure 11. Schematic diagram for estimating encounter number for a linear saddle.**

816

817

818

819



820

821 **Figure 12. u^* -based encounter volume, V^* , for a tracer with an initial distribution south**
822 **the jet and constant meridional gradient north the jet.**

823